Technology

Molecular Cell

A fluorophore-conjugated reagent enabling rapid detection, isolation and live tracking of senescent cells

Graphical abstract

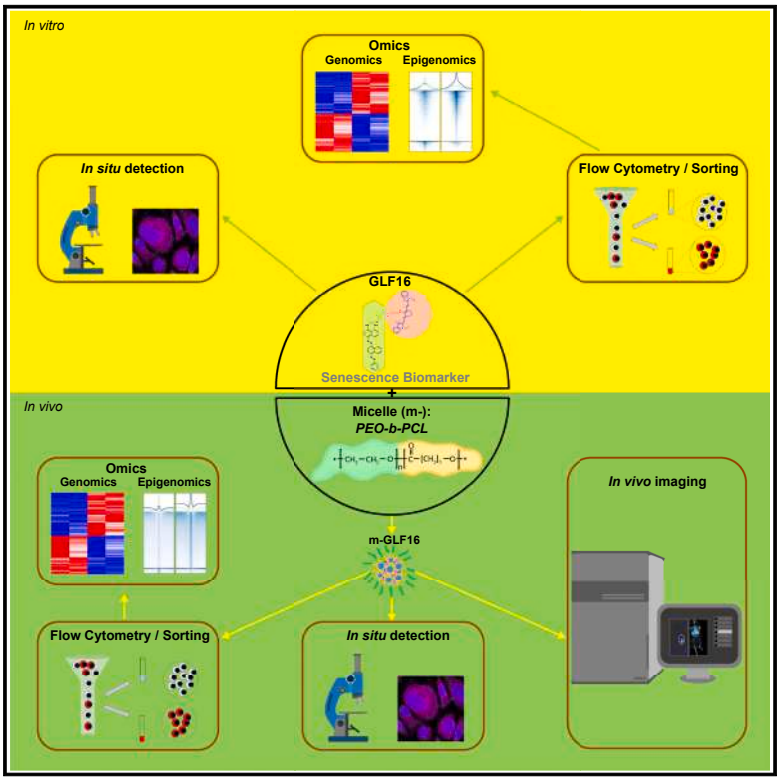

Highlights

- A hydrophilic fluorescent SBB analog (GLF16) robustly identifies senescence
- GLF16 enables rapid flow cytometry and live cell sorting of senescent cells
- GLF16 is successfully encapsulated in a micelle nanocarrier for cell delivery
- A micelle-GLF16 vector tracks live senescent cells *in vivo* and *in vitro*

Authors

Sophia Magkouta, Dimitris Veroutis, Athanasios Pousias, ..., Marco Demaria, Konstantinos Evangelou, Vassilis G. Gorgoulis

Correspondence

vgorg@med.uoa.gr

In brief

Magkouta et al. describe a marker for senescence detection (GLF16) that surpasses limitations of previously established markers (SA-β-Gal and GL13). Apart from *in vitro* analyses, GLF16 is particularly suitable for *in vivo* identification, isolation, and downstream characterization of senescent cell populations at the single-cell level in various biological materials.

Magkouta et al., 2023, Molecular Cell *83*, 3558–3573
October 5, 2023
https://doi.org/10.1016/j.molcel.2023.09.006

CellPress

CellPress

Molecular Cell

Technology

A fluorophore-conjugated reagent enabling rapid detection, isolation and live tracking of senescent cells

Sophia Magkouta,[1,2,22] Dimitris Veroutis,[1,3,22] Athanasios Pousias,[4,22] Angelos Papaspyropoulos,[1,3,22] Natassa Pippa,[5,6] Nikolaos Lougiakis,[4] Konstantinos Kambas,[7] Nefeli Lagopati,[1,3,8] Aikaterini Polyzou,[1] Maria Georgiou,[4] Maria Chountoulesi,[5] Stergios Pispas,[6] Spyros Foutadakis,[3] Nicole Pouli,[4] Panagiotis Marakos,[4] Athanassios Kotsinas,[1] Panayotis Verginis,[3,9,10] Dimitrios Valakos,[3] Athanasia Mizi,[11,12] Argyris Papantonis,[11,12] Giannis Vatsellas,[13] Panagiotis Galanos,[14] Jiri Bartek,[14,15] Russell Petty,[16] Manuel Serrano,[17,18] Dimitris Thanos,[3,13] Charis Roussos,[2] Marco Demaria,[19] Konstantinos Evangelou,[1] and Vassilis G. Gorgoulis[1,3,16,20,21,23,*]

[1]Molecular Carcinogenesis Group, Department of Histology and Embryology, Medical School, National and Kapodistrian University of Athens, 11527 Athens, Greece

[2]Marianthi Simou and G.P.Livanos Labs, 1st Department of Critical Care and Pulmonary Services, School of Medicine, National & Kapodistrian University of Athens, "Evangelismos" Hospital, Athens, 10676, Greece

[3]Biomedical Research Foundation, Academy of Athens, 11527 Athens, Greece

[4]Department of Pharmacy, Division of Pharmaceutical Chemistry, National and Kapodistrian University of Athens, Panepistimiopolis, Zografou, 15771 Athens, Greece

[5]Section of Pharmaceutical Technology, Department of Pharmacy, School of Health Sciences, National and Kapodistrian University of Athens, Panepistimioupolis Zografou, 15771 Athens, Greece

[6]Theoretical and Physical Chemistry Institute, National Hellenic Research Foundation, 11635 Athens, Greece

[7]Hellenic Pasteur Institute, 11521 Athens, Greece

[8]Laboratory of Biology, Department of Basic Medical Sciences, Medical School, National and Kapodistrian University of Athens, 11527 Athens, Greece

[9]Laboratory of Immune Regulation and Tolerance, Division of Basic Sciences, University of Crete Medical School, 70013 Heraklion, Greece

[10]Institute of Molecular Biology and Biotechnology, Foundation for Research and Technology, 70013 Heraklion, Greece

[11]Institute of Pathology, University Medical Center Göttingen, 37075 Göttingen, Germany

[12]Clinical Research Unit 5002, University Medical Center Goettingen, 37075 Goettingen, Germany

[13]Greek Genome Center, Biomedical Research Foundation, Academy of Athens, 11527, Athens, Greece

[14]Genome Integrity Group, Danish Cancer Society Research Center, 2100 Copenhagen, Denmark

[15]Science for Life Laboratory, Division of Genome Biology, Department of Medical Biochemistry and Biophysics, Karolinska Institute, Solna, 171 77 Stockholm, Sweden

[16]Ninewells Hospital and Medical School, University of Dundee, DD19SY Dundee, UK

[17]Institute for Research in Biomedicine (IRB Barcelona), Barcelona Institute of Science and Technology (BIST), 08028 Barcelona, Spain

[18]Altos Labs, Cambridge Institute of Science, Granta Park CB21 6GP, United Kingdom

[19]European Research Institute for the Biology of Ageing (ERIBA), University Medical Center Groningen, 9713 AV Groningen, The Netherlands

[20]Faculty Institute for Cancer Sciences, Manchester Academic Health Sciences Centre, University of Manchester, M20 4GJ Manchester, UK

[21]Faculty of Health and Medical Sciences, University of Surrey, GU2 7YH Surrey, UK

[22]These authors contributed equally

[23]Lead contact

*Correspondence: vgorg@med.uoa.gr

https://doi.org/10.1016/j.molcel.2023.09.006

SUMMARY

Cellular senescence is a stress-response mechanism implicated in various physiological processes, diseases, and aging. Current detection approaches have partially addressed the issue of senescent cell identification in clinical specimens. Effective methodologies enabling precise isolation or live tracking of senescent cells are still lacking. In-depth analysis of truly senescent cells is, therefore, an extremely challenging task. We report (1) the synthesis and validation of a fluorophore-conjugated, Sudan Black-B analog (GLF16), suitable for *in vivo* and *in vitro* analysis of senescence by fluorescence microscopy and flow cytometry and (2) the development and application of a GLF16-carrying micelle vector facilitating GLF16 uptake by living senescent cells *in vivo* and *in vitro*. The compound and the applied methodology render isolation of senescent cells an easy, rapid, and precise process. Straightforward nanocarrier-mediated GLF16 delivery in live senescent cells comprises a unique tool for characterization of senescence at an unprecedented depth.

INTRODUCTION

Cellular senescence is a complex stress-response cellular process and a guardian of cell homeostasis.[1] Senescence may occur in both pathological (i.e., cancer, diabetes)[2–6] and non-pathological settings (i.e., tissue repair) and aging.[7–9] Of note, senescence has been recently established as a hallmark of cancer.[10] Given that almost all cell types may undergo senescence

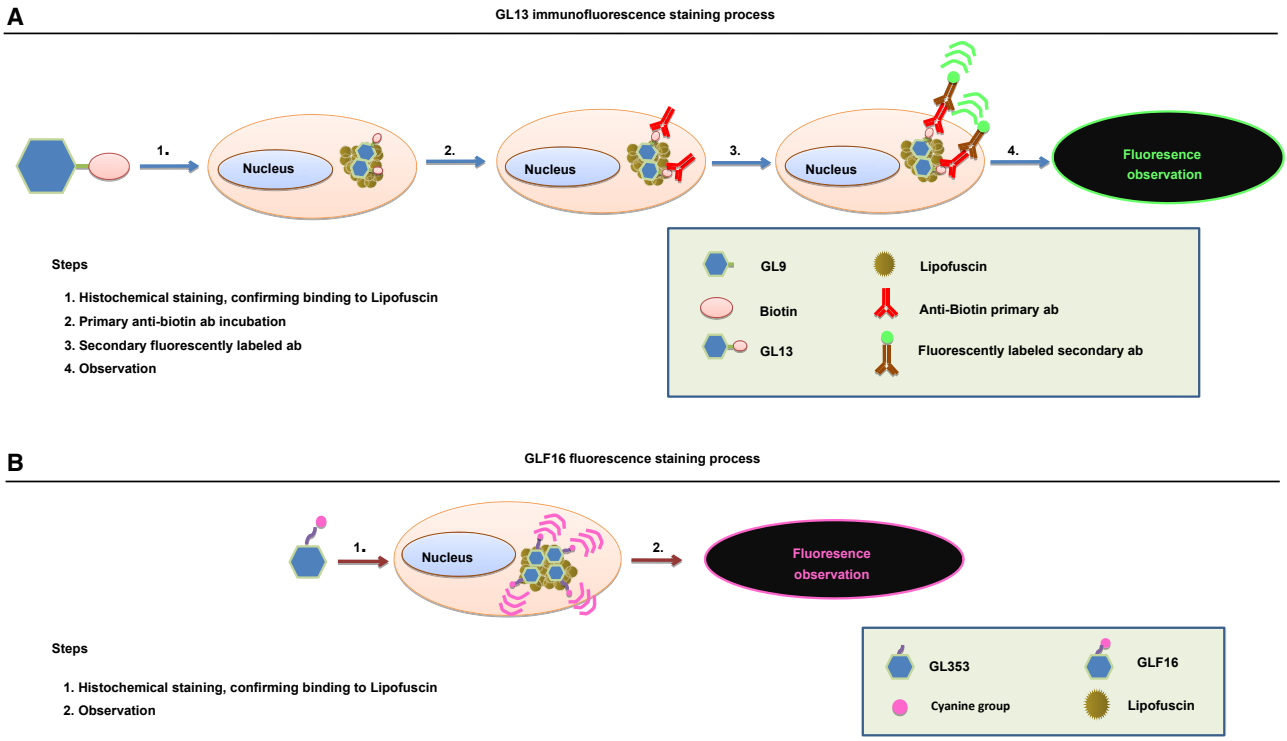

Figure 1. GLF16 enables rapid visualization of senescence in cells and tissues

(A) Identification of senescent cells by applying the lipophilic biotinylated SBB analog GL13 is a three-step process: the GL13-lipofuscin interaction is followed by binding of a primary (anti-biotin ab) and subsequently a secondary antibody that is fluorescently labeled.

(B) GLF16 is already conjugated with a fluorescent moiety and allows visualization of senescent cells in a single step.

accompanied by either beneficial or detrimental outcomes, identification and deep characterization of senescent cells is of paramount importance.

Although cardinal characteristics of senescent cells such as cell cycle arrest, deregulated metabolism, macromolecular damage and the SASP (Senescence-Associated Secretory Phenotype) have been established, the senescent phenotype is largely heterogeneous. Therefore, identification and visualization of senescent cells can be highly challenging, mainly due to the absence of selective and universal markers. Toward this direction we have previously developed a lipophilic, biotin-linked Sudan Black-B (SBB) analog, GL13 (SenTraGor), which allows for precise identification of senescent cells in any biological material (cell cultures, fresh samples, or archival material) based on the detection of lipofuscin accumulating in all senescent cell types.[9,10] Of note, lipofuscin staining using GL13 has been adopted as the first step in the guideline multi-marker algorithm for accurate detection of senescent cells recently proposed by the senescence community.[1,5,11]

Nevertheless, GL13 needs to be diluted in ethanol, and thus, the corresponding staining method encompasses consecutive de- and re-hydration steps, a process which is suboptimal for applications such as flow cytometry-based quantification or isolation of senescent cells.[11] This limitation renders the assay less compatible with several types of downstream analysis of distinct cell populations that would enable a substantially deeper characterization of senescent cells, including genetic, epigenetic (e.g., Chromatin Conformation Capture, 3C techniques) and transcriptomic (e.g., single cell or bulk RNAseq) analyses.[11] Additionally, although GL13 is suitable for immunofluorescence, staining with GL13 is a two-step process that requires a conjugated secondary antibody, and the several washing steps may result in loss of material, especially in low-attachment cell lines.

Design

To overcome these caveats, we herein present the development of an optimized SBB analog conjugated with a fluorophore moiety. The presence of the fluorophore group in the structure of the synthesized compound termed GLF16 renders the compound suitable for fluorescence microscopy and flow cytometric analysis of senescent cells in material from both cell cultures and tissues, while combining the following advantages. (1) The incorporation of a polar side chain between the SBB core and the fluorophore moiety offers GLF16 enhanced aqueous solubility compared to GL13, overcoming thus the aforementioned impediments related to ethanol and enabling its application in bioimaging.[12] (2) It exhibits strong chemical affinity with lipofuscin. (3) It displays a long excitation wavelength (>500 nm, near infrared-NIR) that is less harmful for biological samples and limits background emission from autofluorescent molecules such as lipofuscin. (4) NIR wavelengths diminish light scattering in tissue, yielding higher penetration of the excitation light. (5) It can be

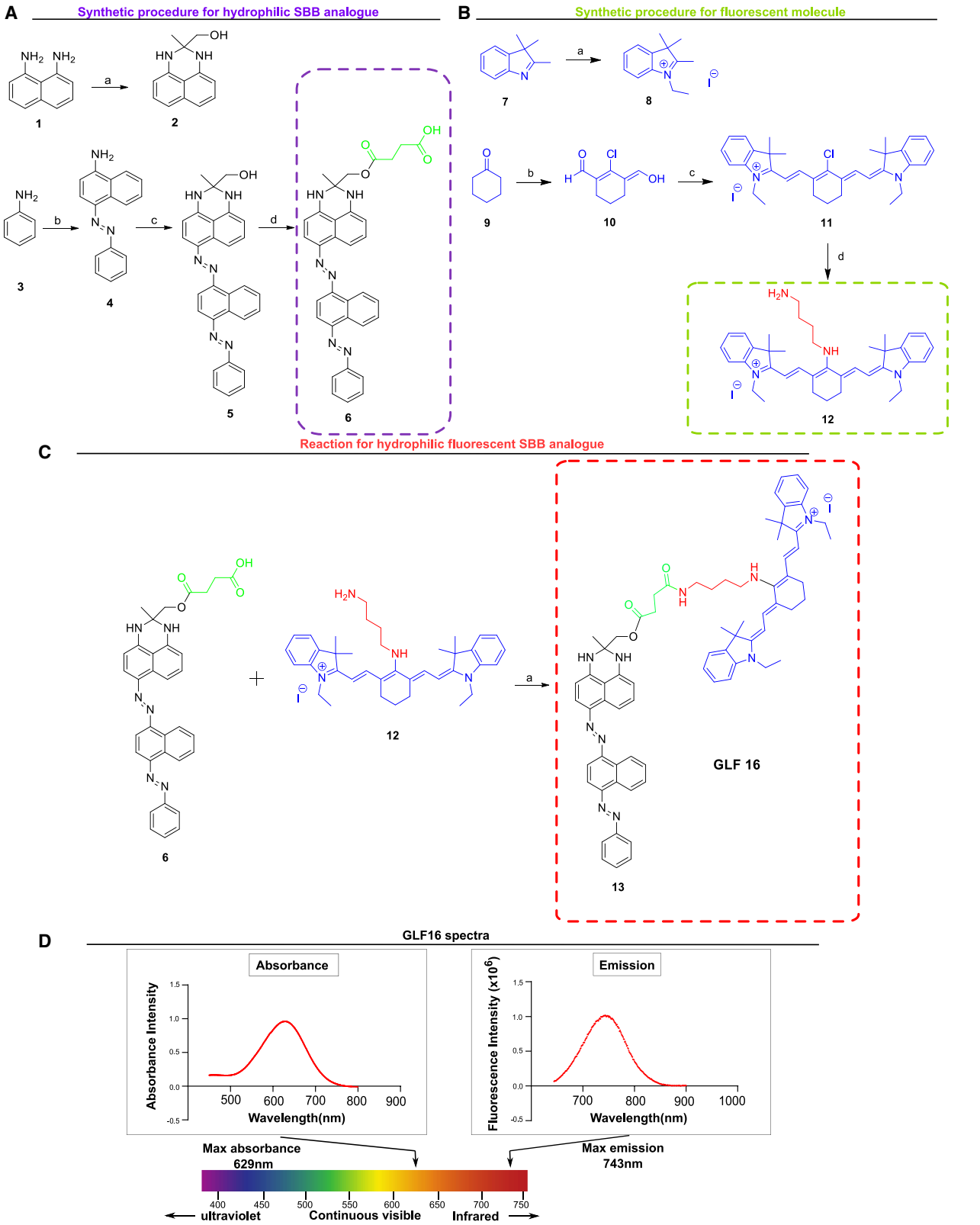

(legend on next page)

used at low concentrations minimizing toxicity but with easier detection as it produces high-intensity output. We validated the specificity and properties of GLF16 in established for senescence cellular systems previously developed by our group[13,14] as well as in tissues previously shown to harbor (positive controls) or to be devoid (negative controls) of senescent cells.[11,15]

Importantly, a major advantage of the GLF16 compound that is anticipated to revolutionize the senescence field stems from the fact that following its encapsulation in a suitable nanocarrier, efficient introduction and release into living cells was achieved allowing its interaction with lipofuscin and eventually, for the first time, tracing live senescent cells.

RESULTS

Design, synthesis, and characterization of hydrophilic SBB analogs

Using GL13 as the template molecule, we synthesized a number of non-biotinylated, SBB analogs carrying different fluorescent moieties in order to achieve high-intensity output (Figure S1A, Methods S1). We subsequently tested the chemical affinity of the analogs with lipofuscin using cells with high lipofuscin levels.[15] GLF16 was selected as the most effective analog, as it masked lipofuscin autofluorescence and simultaneously displayed the strongest signal at NIR wavelengths, assessed by fluorescence microscopy (Figures 1 and S1B).

GLF16 is an SBB analog conjugated with a fluorophore moiety (cyanine heptamethine group, blue) through a succinic linker (green) and a polar 1,4-diaminobutane group (red) (Figures 2A–2C). The main steps of GLF16 synthesis were the following (see Methods S1 for details): 1,8-diaminonapthalene (1) was converted to the bis-diazenyl analog (5) through a three-step synthetic procedure, described previously by our group,[15] which yielded the succinic ester (6), upon treatment with succinic anhydride (Figure 2A). In parallel, for the production of the fluorescent molecule, 2,3,3-trimethyl-3H-indole (7) was used as the starting material and was converted to a cyanine chlorointermediate (11) through a three-step synthetic procedure.[16] Treatment of the latter with 1,4-diaminobutane led to the aminosubstituted cyanine derivative (12) (Figure 2B). Finally, a coupling reaction of the cyanine derivative (12) with the succinic SBB analog (6) resulted in the target fluorophore-conjugated compound GLF16 (Figure 2C).

Three additional analogs with similar structure were synthesized, namely GLF7, GLF19 and GLF21, where the 1,4-diaminobutane group was replaced with the polar piperazine moiety or the less polar 4-hydroxyphelylamino and 4-aminophenoxy groups, respectively (Figure S1A). Among the several reported fluorophore groups that could be used for incorporation into the currently described derivatives, such as the xanthine-based fluorophores (fluorescein, rhodamines, and eosins) or the BODIPY (boron dipyrromethene difluoride) derivatives, we chose the cyanine heptamethine moiety since it displays an excitation wavelength of >600 nm in the near-infrared region (NIR). NIR wavelengths require lower energy for excitation, are less harmful for biological samples,[12] and diminish light scattering in tissue, yielding higher penetration and limiting background emission from autofluorescent molecules, such as lipofuscin. GLF16, GLF7, GLF19, and GLF21 were characterized by ^{1}H and ^{13}C NMR spectroscopy and by high resolution mass spectroscopy (HRMS) (Methods S1).

GLF16 was generated to be hydrophilic via (1) the addition of the basic polar 1,4-diaminobutane side chain, which can easily be ionized at pH < 8, and (2) the presence of the charged nitrogen atom of the cyanine group. When dissolved in a PBS buffer solution containing minimum amounts of DMSO (2.5%) and Tween 20 (2.5%), GLF16 exhibits strong absorbance with a maximum at 629 nm as well as fluorescence with an emission maximum at 743 nm (Figure 2D). Consequently, GLF16 demonstrated a large Stokes shift (114 nm), which is a favorable characteristic for fluorescent derivatives with potential biomedical applications.[17]

GLF16 successfully identifies senescent cells in senescence model systems

In order to examine the ability of GLF16 to accurately stain senescent cells, we used several *in vitro* and *in vivo* model systems established to study senescence, as well as clinical material with previously characterized senescence status. Particularly, we implemented previously described cellular systems, animal models, young versus aged tissues, as well as tissues subjected to various senescence-inducing treatments against their corresponding non-senescent controls[11,13–15] (Figure S2).

Abundant positive GLF16 staining was observed in the doxycycline-induced cell lines (Li-Fraumeni-p21$^{WAF1/Cip1}$ Tet-ON and HBEC-CDC6 Tet-ON cellular systems), while it was almost absent in untreated cells (Figures 3A, 3D, 3E, 3H, S1B, S3A, and S3B). Importantly, GLF16 staining was clearly similar to the one obtained with GL13 (Figures 3A, 3E, and S3C–S3F).

To further evaluate the specificity of the compound and following the algorithm for precise assessment of senescent cells[1,11] we co-stained GLF16 and p16^{INK4A}, p21$^{WAF1/Cip1}$ (Figures 3B, 3D, 3F, 3H, S4A, and S4B), or Ki67 (Figures 3C, 3D, 3G, 3H, S4A, and S4B). As expected, GLF16 overlapped with p21$^{WAF1/Cip1}$ and p16^{INK4A} staining but exhibited a mutually exclusive pattern with Ki67. In addition, we tested the compatibility of GLF16 co-staining with the EdU ClickIT method to assess senescent events coupled with cell cycle profiling through high-content microscopy, based on the quantitative image-based cytometry (QIBC), as previously described.[18] Oncogene overexpression (CDC6 activation) abolished DNA

Figure 2. Chemical synthesis procedure and physical properties of GLF16

(A–C) Synthetic procedure for GLF16. 1,8-diaminonapthalene (1) was converted to the bis-diazenyl analog (5) through a three-step synthetic process (2–4). A succinic group was inserted in (5) to serve as a coupling site for the fluorophore, resulting in the SBB analog GL353 (6). The fluorescent cyanine derivative GLF15 was synthesized (12) and subsequent coupling of the latter to GL353, through an amide bond eventually led to the GLF16 product. Detailed description of the conditions of all chemical reactions is provided in Methods S1.

(D) Absorbance and emission Spectra of GLF16 solution in aqueous PBS buffer (95% PBS, 2.5% DMSO, 2.5% Tween 20). Concentration of GLF16 used for measurements was 2 μM for absorbance and 13.3 μM for fluorescence, respectively.

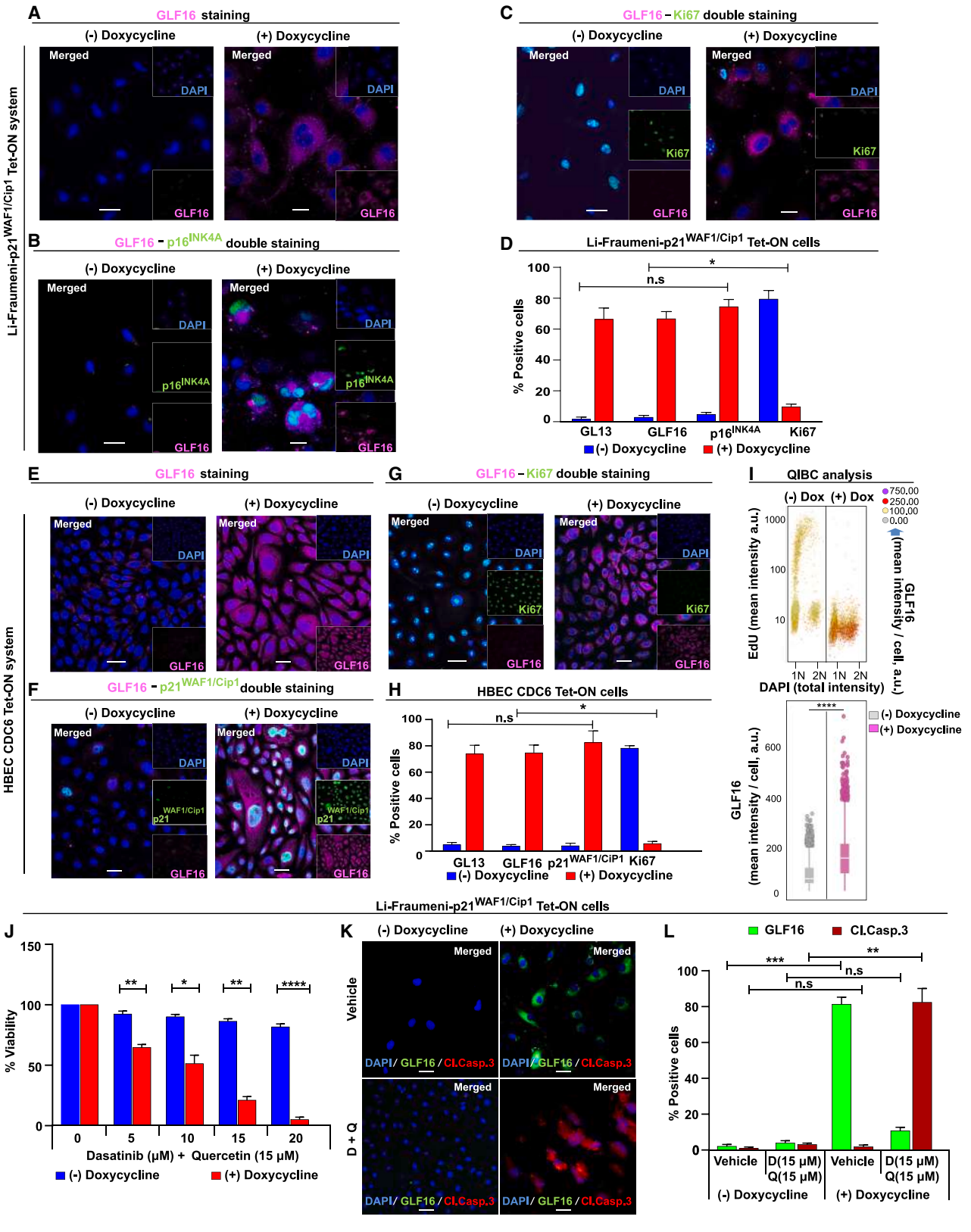

(legend on next page)

replication, while GLF16 intensity appeared heavily augmented (Figure 3I), supporting the employment of GLF16 to detect senescent cells with high-content microscopy for the very first time. Finally, following treatment with a combination of senolytic drugs (Dasatinib and Quercetin) (Figures 3J, S4C, and S4D), high levels of apoptosis were observed, as indicated by cleaved caspase 3 staining, whereas the percentage of GLF16-positive cells became negligible, further verifying the specificity of GLF16 in identifying senescent cell populations (Figures 3K, 3L, and S4E).

We next evaluated the efficacy of GLF16 in tissue samples harboring variable lipofuscin levels. GL13 staining in serial sections from human seminal vesicles and aged liver served as positive control, and importantly, GLF16 detected the same lipofuscin-positive cells in those sections (Figure S3E). Of note, GLF16 staining conferred a stronger signal intensity compared to GL13, but comparable staining indices (Figures S3E and S3F).

We then stained various clinical and pre-clinical (mouse) biospecimens previously shown to harbor senescent cells[11,15] against GLF16. Positive (senescent) cells, even when present at low numbers, were identified in human tissues from irradiated head and neck carcinomas, chemotherapy-treated breast and aged liver (Figures 4A–4C and S4F), as well as in mouse lesions from K-ras^{V12}-induced mouse lung adenomas, palbociclib-treated melanoma xenografts, and bleomycin-induced lung fibrosis (Figures 4D–4F and S4F). In contrast, in corresponding negative control tissues, no staining was evident, further highlighting the sensitivity and specificity of the compound. Finally, GLF16 specificity was also evaluated in the same settings by GLF16 co-staining with p16^{INK4A} and p21$^{WAF1/Cip1}$ or Ki67 (Figures 4G–4I and S4G). Overall, these results render GLF16 staining an effective approach for accurate detection of senescent cells in cell culture and tissue material, while importantly, following a simple, one-step, straight-forward experimental procedure.

GLF16 enables efficient isolation of senescent cells by flow cytometry

A major conundrum in the senescence field relates to the isolation of pure senescent cell populations. Flow cytometric analysis of senescent cells using SA-β-gal or cell surface markers such as urokinase-type plasminogen activator receptor (uPAR) and dipeptidylpeptidase 4 (DPP4) have been reported.[19–21] However, those methodologies can only be performed in fresh samples or samples of specific cancer types and frequently yield false positive or false negative results.[11] In addition, the use of ethanol in GL13 solutions may substantially modify protein epitopes and can lead to a significant loss of cells due to the high number of washing steps required.[11] The optimized properties of GLF16 eliminate the requirement for consecutive ethanol de-hydration and subsequent re-hydration steps.

We tested GLF16 efficacy in flow cytometry (detailed conditions are available in the corresponding STAR Methods sections) in the Li-Fraumeni-p21$^{WAF1/Cip1}$ (Figures 5A–5C and S5A) and HBEC CDC6 Tet-ON (Figures S5B and S5C) cellular systems. GLF16 was able to discriminate senescent against non-senescent cells in both naive and induced (Doxycycline-treated) cells (Figures 5B and S5B). GLF16 (+) populations were found p16^{INK4A}-positive and Ki67-negative, while GLF16 (−) populations displayed the exact opposite staining pattern [Ki67 (+)/p16^{INK4A} (−)] (Figures 5B, 5C, S5B, and S5C). We then used GLF16 in primary T cell cultures that were treated with cisplatin, an agent conferring DNA damage (Figures S5D and S5E). Cisplatin-treated T cell populations exerted a GLF16 (+)/p16^{INK4A} (+) staining pattern while naive T cells were double-negative (Figure S5D). Taken together, our findings support the implementation of GLF16 for rapid multimarker analysis of senescent cells as well as senescent cell sorting using fluorescence-activated cell sorting (FACS). Most importantly, GLF16 was found to successfully discriminate senescent against non-senescent cells as verified by subsequent RNAseq analysis of sorted GLF16 (+) versus GLF16 (−) cells. Senescence-associated genes[1] were found to be highly expressed in GLF16 (+) cells compared to GLF16 (−) ones (Figure 5D). These results were also complemented by a ChIP-seq analysis using the active transcription H3K27ac histone marker (Figure 5E), demonstrating a significant overlap between H3K27ac-enriched enhancers and upregulated gene transcripts as identified in our RNA-seq analysis (Figures S5F and S5G). In contrast, repressed H3K27ac peaks significantly overlapped with downregulated transcripts (Figures S5F and S5G). Thus, GLF16 allows for sorting of

Figure 3. Detection of senescent cells by GLF16

(A–D) Li-Fraumeni-p21$^{WAF1/Cip1}$ Tet-ON cells treated or not with Doxycycline for 6–8 days were fixed, permeabilized, and stained with GLF16 (A). GLF16 staining resulted in an intense cytoplasmic signal (corresponding to lipofuscin aggregates) abundant in senescent cells and entirely absent in untreated ones.

(B) GLF16 specificity was subsequently evaluated by co-staining with anti-p16^{INK4A}, a marker commonly linked with senescence.

(C) Specificity of GLF16 was further evaluated by co-staining with the proliferation marker Ki67. An inverse relationship between GLF16 and Ki67 positivity was depicted.

(D) Quantification of the percentage of positive cells after staining with the indicated markers depicted as means ± SD from six independent experiments. Images were acquired using a confocal microscope equipped with a digital camera and positive cells were evaluated by two independent readers.

(E–H) Similar experimental approach as in (A)–(D) was followed using the HBEC CDC6 Tet-ON cellular system.

(I) Results from quantitative image-based cytometry (QIBC) in HBEC CDC6 Tet-ON cells at the indicated timepoints, depicting cell cycle distribution based on EdU incorporation and DAPI levels (a.u., arbitrary unit). GLF16 mean intensity per cell is indicated by color coding.

(J) Li-Fraumeni-p21$^{WAF1/Cip1}$ Tet-ON cells treated or not with Doxycycline for 6–8 days and then for 3 days with Dasatinib (0–20 μM) and Quercetin (15 μM) or vehicle. Cell viability was assessed by MTT assay. Results are expressed as means ± SD, percentage of vehicle, n = 3.

(K) Cells from (J) treated with vehicle or Dasatinib and Quercetin (D + Q) were fixed and co-stained for the apoptosis marker Cl.Caspase-3 and GLF16 for identification of senescent cells.

(L) D + Q-treated doxycycline-induced cells show decreased levels of GLF16 and increased levels of Cl.Caspase-3, opposite to vehicle-treated cells (Cl, cleaved). An inverse relationship between GLF16 and Cl.Caspase-3 positivity is depicted. Bar graphs show Cl: Capase-3 or GLF16 mean intensity per cell alone. Dox, Doxycycline. *p < 0.05, **p < 0.01, ***p < 0.001, ****p < 0.001 compared to respective controls based on Kruskal Wallis Test. Objectives 20×, 40x. Scale bars, 10 μm (A–C) and 25 μm (E–G, K).

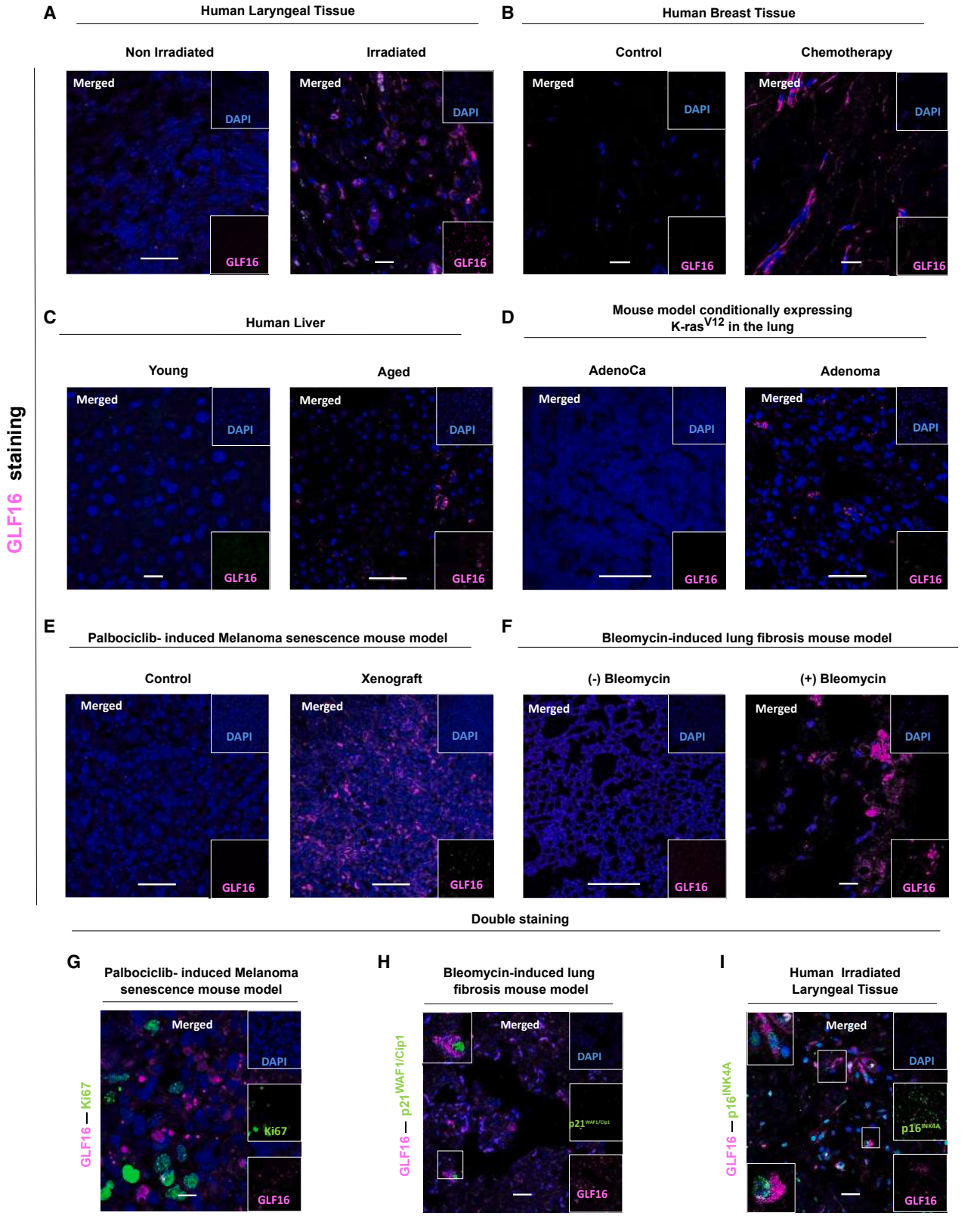

(legend on next page)

senescent cells and subsequent state-of-the-art transcriptomic and epigenetic analyses, enabling the gain of substantially deeper insights into the biology and functions of senescent cells of any type.

Development of a micelle-embedded GLF16 for live cell delivery and isolation

Although structurally optimized with the presence of the fluorescent cyanine group and the polar 1,4-diaminobutane side chain, the GLF16 reagent still exerts considerable lipophilicity (hydrophobic properties), which is imperative for its interaction with lipofuscin but, on the other hand, requires a minimum amount of DMSO and Tween 20 additives to be fully dissolved in aqueous media. This was a major issue to be addressed in order to employ this derivative for *in vivo* experiments and potential biomedical applications.

To bypass this challenge, we generated a PEO-b-PCL copolymer (micelle) carrying GLF16, (from now on termed m-GLF16) (Figures 6A–6C). The PEO-b-PCL copolymer was selected based on its well-known biocompatibility and biodegradability properties, rendering it the material of choice for the encapsulation of hydrophobic compounds. Initially, efficient incorporation of GLF16 into the PCL core was tested by preparing in parallel pure PEO-b-PCL micelles and comparing them with the corresponding m-GLF16 ones. Indeed, while the size (D_h) of pure PEO-b-PCL micelles was estimated at 95 nm, addition of the GLF16 led to increase of the D_h at 110 nm, indicating successful incorporation (Methods S3). Next, m-GLF16 was administered in living Li-Fraumeni-p21$^{WAF1/Cip1}$ Tet-ON senescent cells and their non-senescent counterparts, in order to investigate whether GLF16 can be successfully delivered into live cells, eventually interacting with lipofuscin (Figures 6D, 6E, S6B, and S6C). A strong GLF16 cytoplasmic signal that coincided with p16^{INK4A} immunopositivity and lack of Ki67 expression, was evident within doxycycline-treated cells, while it was totally absent in the untreated counterparts (Figures 6E-bottom panel, S6B, and S6C). Notably, application of pure PEO-b-PCL copolymer in these cells resulted in absence of any fluorescent signal (Figure S6A). Flow cytometry analysis in living cells of the same cellular system, sorted the cells based on GLF16 fluorescence (Figure 6E-upper panel). Subsequent RNA-seq and H3K27ac ChIP-seq analysis of the cells that incorporated m-GLF16 revealed a strong fingerprint of the senescence gene signature[1] (Gorgoulis et al., 2019) compared to GLF16 (−) ones (Figures 6F–6I). These findings demonstrate successful delivery of the GLF16 reagent, via m-GLF16 incorporation and subsequent release in living cells. Moreover, given that GLF16 strongly interacts with lipofuscin aggregates, senescent cells may be faithfully identified versus their non-senescent counterparts.[22] Taken together, the synthesis and implementation of the m-GLF16 micelle may allow for accurate isolation and subsequent culturing and tracking of live senescent cells.

In order to further validate the efficiency of our *m*-GLF16 compound in labeling senescent cells in a 3D cellular system, *m*-GLF16 was additionally delivered in airway organoids we generated directly from healthy lung tissues[23] (Figure 7A). Patient-derived organoid (PDO) cultures are able to recapitulate tissue architecture and function more faithfully than any other *in vitro* system developed so far.[24,25] Given that until now it has been impossible to monitor cellular senescence directly in human patients, incorporation of m-GLF16 into live PDOs may offer a unique opportunity to overcome the existing limitations. To that end, we induced hydrogen peroxide (H_2O_2)-mediated senescence[26] in our airway organoids, applied subsequently m-GLF16, and monitored senescence via immunofluorescence. As expected, compared to control cultures, H_2O_2-treated organoids exhibited increased senescence as indicated by a relatively enlarged cell size, increased p21$^{WAF1/Cip1}$ and decreased Ki67 expression (Figures 7B and 7C). Importantly, GLF16 (+) cells were detected only upon H_2O_2 treatment, overlapping with p21$^{WAF1/Cip1}$ staining (Figures 7B and 7C), validating the successful delivery of m-GLF16 in airway PDOs. As expected, GLF16 and p21$^{WAF1/Cip1}$ positivity did not coincide with Ki67 positivity (Figures 7B and 7C). This finding is of high importance, as implementation of m-GLF16 may enable the study of senescence in human patients at a personalized level.

Having successfully detected senescent cells in 2D and 3D cell cultures, we subsequently examined the potential of m-GLF16 in tracing senescent cells in living organisms. We therefore proceeded to live imaging in two well-established murine senescence models, particularly the palbociclib-treated murine melanomas[27] and the bleomycin-induced lung fibrosis models[28] (Figure S6D). In both, a robust fluorescence signal was detected 24 h following m-GLF16 administration in the senescent regions (Figures 7D and 7E). Similarly, a strong signal was observed when palbociclib-treated tumors and bleomycin-treated lungs were imaged *ex vivo* (Figures 7F and 7G). The fluorescence signal observed in the liver in both animal models stems from the fact that this organ is the site of metabolic processing of exogenous substrates. GLF16 immunofluorescence confirmed high numbers of senescent cells within the tumors and fibrotic lungs and absence of senescent cells in the rest of the organs, further verifying the specificity of the signal (Figures 7H, 7I, and S6E). Importantly, no histopathological alterations in vital organs

Figure 4. *In situ* detection of senescent cells by applying GLF16

Representative images of GLF16 staining in human clinical settings and murine systems, known to harbor an increased burden of senescent cells, and respective negative controls (devoid of senescent cells) are depicted.

(A–F) Irradiated human laryngeal tissues, (B) chemotherapy-treated breast tissues and (C) liver specimens from aged individuals were abundant in GLF16-positive cells, whereas in respective controls, these positive cells were totally absent. Similar results were obtained in the following murine models: (D) K-ras^{V12}-induced lung adenomas, (E) palbociclib-treated human melanoma xenografts, and (F) bleomycin-induced lung fibrosis.

(G–I) GLF16 specificity and sensitivity was subsequently evaluated by concurrent staining with the proliferation marker Ki67 or senescence-associated markers p21$^{WAF1/Cip1}$ and p16^{INK4A}. GLF16 staining coincided with p16^{INK4} or p21$^{WAF1/Cip1}$ but not with Ki67. Lipofuscin (GLF16) positive macrophages in bleomycin-treated lungs are also evident (H), as previously demonstrated in Evangelou et al., 2017.[15] Objectives 10×, 20x, 40x, 63x. Corresponding scale bars are depicted. Scale bars, 50 μm (A-F), 10 μm (G), and 25 μm (H-I).

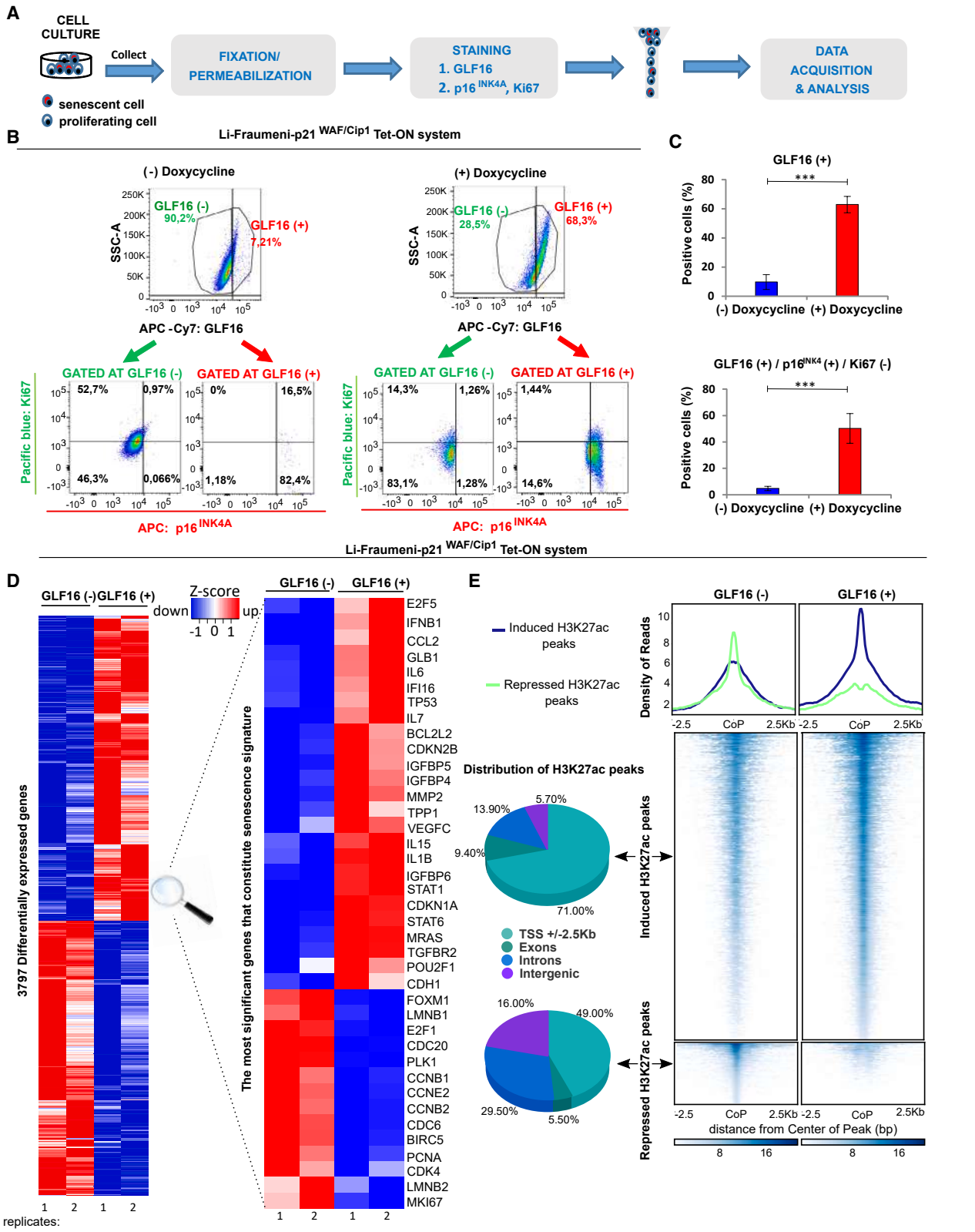

(legend on next page)

of the animals that received an overdose of *m*-GLF16 (Figure S6F) and no differences in total or differential white blood cell counts were observed, suggesting a low toxicity profile (Figure S6G).

DISCUSSION

In this report, we demonstrate that our fluorescently labeled GLF16 compound enables robust characterization (by fluorescence microscopy) and efficient senescent cell isolation (by flow cytometry) from a variety of biological samples by applying a fast and accurate one-step methodology on fixed and permeabilized cells. The development of a live cell delivery platform that would substantially increase the solubility and ameliorate the absorption, metabolism, distribution, excretion, and toxicology [ADME(T)] profile[29] of GLF16 was the second goal of this study. The selected PEO-b-PCL nano-carrier can facilitate GLF16 delivery, allowing isolation (via FACS), culturing, tracking (via fluorescence), and high-throughput downstream analysis (integrated multi-omics) of living senescent cells in *in vitro* and *in vivo* settings. This constitutes a major advance over previous broadly used reagents and assays, such as SA-β-Gal, whose use is accompanied by frequent false positive/negative outcomes, or even our recently established lipofuscin-identifying lipophilic reagent GL13, which requires dilution in ethanol.[11]

GLF16 displays high sensitivity due to its strong affinity with lipofuscin. Therefore, GLF16 is not only potent in identifying cells artificially induced to undergo senescence where the signal is naturally stronger, but it can be additionally used to sort spontaneously and/or rare-to-find senescing cells in cell cultures or tissues. This is an important property of GLF16, as spontaneously senescent cells have been found in several contexts, including untreated normal and cancer cell lines and tissues.[30,31] Interestingly, GLF16 is anticipated to address the issue of in-depth characterization of such populations, unfeasible until now due to the lack of appropriate and efficient methodologies.

Senescent cells have been shown to create an immunosuppressive tissue microenvironment[32] and contribute to cancer cell progression *in vitro* and *in vivo*.[33] A question that remains poorly addressed, partly due to the absence of suitable senescence biomarkers, is whether immune cells may display senescence as a consequence of their interaction with cancer cells and what the underlying mechanisms of immune cell senescence are. Given that immune cell (sub)population sorting has traditionally relied on flow cytometry-based approaches, the use of an optimized compound such as GLF16 would, for the first time, unlock the possibility to faithfully distinguish senescent from non-senescent immune cell populations. Transcriptional and chromatin conformation analyses of sorted immune cells would yield invaluable information on the senescent programs in place.

The polymeric m-GLF16 system we developed is suitable for endocytosis due to its nanoscale size. The co-polymer that was utilized, is well-known for its biocompatibility and biodegradability properties, being ideal for biomedical applications.[34–36] Its degradation within the acidic environment of the cytoplasm leads to release of the compound from the core of the micelle, eventually permitting its interaction with lipofuscin aggregates and labeling of live senescent cells *in vitro*.[37,38]

Interestingly, m-GLF16 enables tracking, isolation and culturing of living senescent cells for various downstream applications. Along these lines, we show that m-GLF16 successfully tracks senescent cells in human airway organoids. The importance of this finding lies in the fact that organoids are highly complex 3D culture systems (consisting of various cell types grown in ECM), thereby closely recapitulating histological and functional features of the organ they originate from,[23] and constitute a vital tool for personalized disease-modeling.[25] A tool such as m-GLF16 for monitoring senescence directly at the patient level was so far missing from the field, posing considerable limitations in the translation of senescence-related research. Apart from the multiple aforementioned applications of m-GLF16 in *ex vivo* settings, we additionally demonstrate that m-GLF16 can be successfully delivered within senescent cells in living organisms, allowing their real-time monitoring and isolation. Importantly, intravenous injection of the carrier is well tolerated by animals, and therefore, multiple real-time and long–term measurements are feasible without having to terminate the experimental processes (compatible with the 3Rs principle [replacement, reduction, and refinement] in animal testing). Taking into account all the above, m-GLF16 emerges as a pioneering tool for investigations in humans, paving the way for imaging and in-depth analysis of senescence in a wide spectrum of human pathologies.

Besides SASP, senescent cells may exhibit detrimental properties by escaping from senescence under certain circumstances.[13,18] Thus, the field of senotherapeutics, aiming to deal with those adverse effects, is anticipated to drastically benefit from such interventions. In this context, linking GLF16 with a senolytic drug that "kills" senescent cells through construction of a micellar [m-GLF16-senolytic] system emerges as an attractive strategy for senescent cell selective removal. It is clear that similar *in vivo* approaches are now closer than ever and are expected not only to significantly improve our understanding of the role of

Figure 5. GLF16 enables efficient identification, quantification, and multimarker analysis of senescent cells by flow cytometry

(A) Experimental workflow implemented.

(B and C) Flow cytometry analysis of Li-Fraumeni-p21$^{WAF1/Cip1}$ Tet-ON cells with or without Doxycycline treatment. Cells were stained with GLF16, anti-p16^{INK4A}-APC, and anti-Ki67-Pacific blue. Gating of GLF16 (+) and GLF16 (−) cells subsequently verified co-detection of GLF16 and senescence markers (p16^{INK4A} positivity and absence of Ki67) in the senescent population (induced cells), whereas the opposite pattern was observed in the non-treated ones. Data presented as mean ± SD from three independent experiments. ***$p < 0.001$ compared to (−) doxycycline by two-tailed Student's *t* test.

(D) Left panel: heatmap depicting the differentially expressed genes (DEGs) of sorted GLF16 (+) against GLF16 (−) cells. Right panel: part of the DEGs heatmap displaying the most significant senescence signature genes (DEGs cut-off: Log2 fold change 0.5, p value < 0.05).

(E) Left panel: Pie charts showing the genomic distribution of the accessible regions of induced and repressed H3K27ac ChIP-seq peaks. Right panel: density heatmaps of the differentially accessible regions of sorted GLF16 (+) against GLF16 (−) cells. The reference point for the plotting is the center of the peaks (CoP), with distance 2.5 kb downstream and upstream of the peaks.

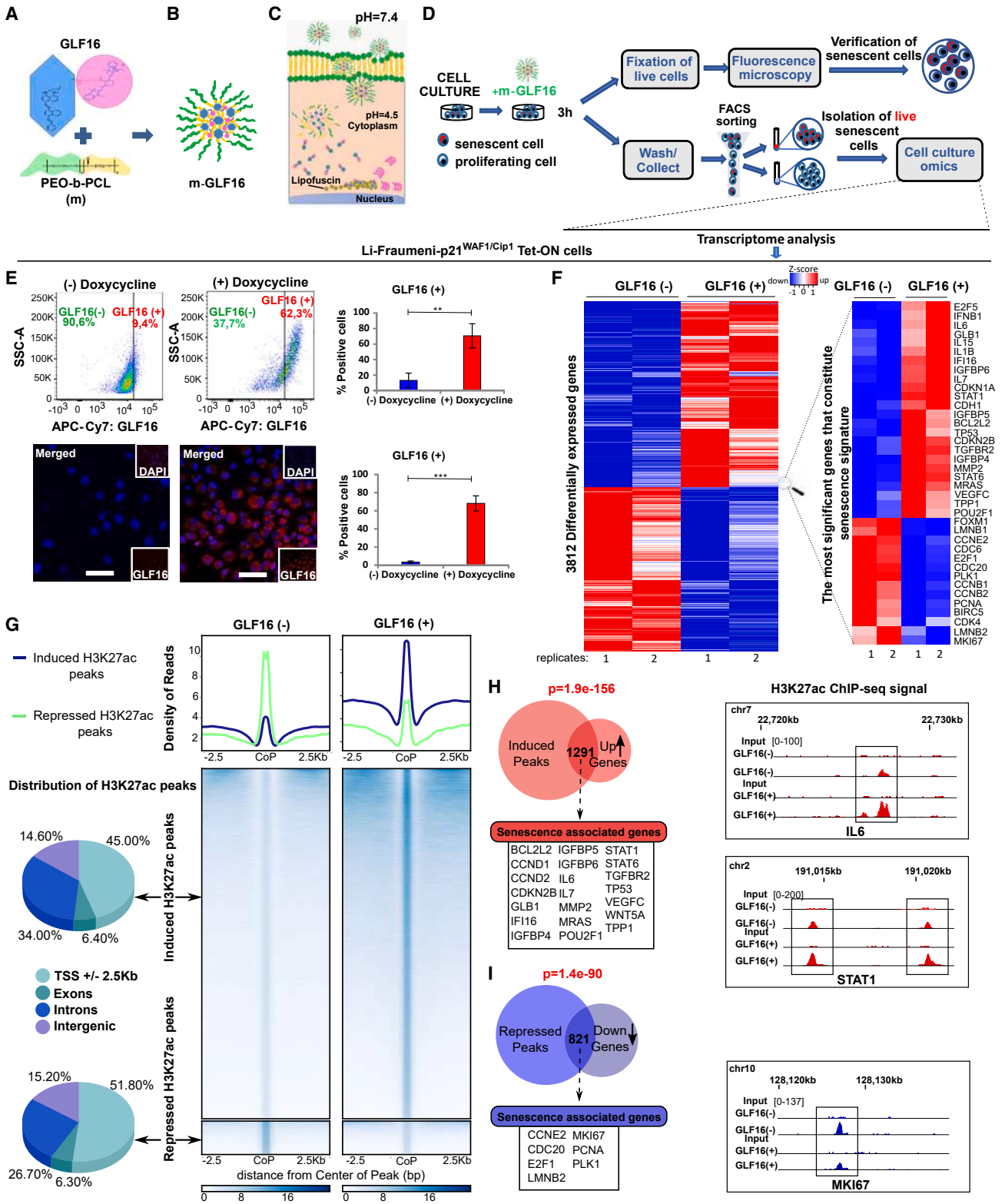

Figure 6. Live cell delivery of *m*-GLF16 enables isolation of living senescent cells

(A and B) Development of micelle-based GLF16. GLF16 was successfully embedded in a PEO-b-PCL copolymer, where PEO is the hydrophilic and PCL the hydrophobic part of this micelle, forming a delivery platform.

(legend continued on next page)

cellular senescence in living organisms, but importantly, to develop effective strategies to precisely eliminate its adverse effects. Toward this direction, extremely valuable properties of the *m*-GLF16 delivery system affecting its degradation process, release and circulation time can be occasionally manipulated in order for GLF16 to reach its targets within tissues and organs in future *in vivo* applications. Thus, further *m*-GLF16 optimization is among our perspectives, by adjusting crucial parameters such as the length of PEO, the external hydrophilic layer of micelles that makes the nanoparticulate delivery system unperceivable to phagocytic cells, avoiding the aggregation with albumin and other serum proteins, thus increasing the circulation time in the plasma.[39]

Limitations of the study

Regardless of the nature of the available material (FFPE, fixed, non-fixed/live cells) the only limitation of GLF16 is related to the fact that a fluorescence microscope with appropriate filter (infrared) and camera is required. Furthermore, it should be mentioned that *m*-GLF16 should be used within a short period of time post preparation to ensure maximum efficiency.

Taken together, the pioneering properties of GLF16 render it a valuable tool in the senescence field, unlocking key experimental approaches that are anticipated to further boost our knowledge on various aspects of cellular senescence and particularly its role in human diseases, which have been so far deemed unfeasible.

STAR★METHODS

Detailed methods are provided in the online version of this paper and include the following:

- KEY RESOURCES TABLE
- RESOURCE AVAILABILITY
  - Lead contact
  - Materials availability
  - Data and code availability
- EXPERIMENTAL MODEL AND STUDY PARTICIPANT DETAILS
  - Models
  - *In vitro* models
  - *In vivo* models
- METHOD DETAILS
  - GLF16 chemical synthesis
  - GLF16 solution preparation
  - Immunofluorescence analysis
  - Flow cytometry
  - QIBC analysis
  - Treatment with senolytics
  - Nano-delivery system
  - Tracking of living senescent cells in human airway organoids using *m*-GLF16
  - Visualization of senescent cells *in vivo*
  - RNA and ChIP-sequencing analysis of fixed or live FACS-sorted cells
- QUANTIFICATION AND STATISTICAL ANALYSIS
- ADDITIONAL RESOURCES

SUPPLEMENTAL INFORMATION

Supplemental information can be found online at https://doi.org/10.1016/j.molcel.2023.09.006.

ACKNOWLEDGMENTS

The authors would like to acknowledge Dr Ioannis Dotsikas and Dr Elena Charalampous who performed the absorbance and fluorescence measurements and Dr. Nikolaos Spyridon Boukos for TEM image acquisition.

Funding: We acknowledge support by the National Public Investment Program of the Ministry of Development and Investment/General Secretariat for Research and Technology, in the framework of the Flagship Initiative to address SARS-CoV-2 (2020ΣΕ01300001); the European Regional Development Fund of the European Union and Greek national funds through the Operational Program Competitiveness, Entrepreneurship, and Innovation, under the call RESEARCH–CREATE–INNOVATE (project codes: T2EDK-02939 and T2EDK-03266); Sonia Kotopoulos donation; Hellenic Foundation for Research and Innovation (HFRI) grant 3782 and NKUA-SARG grant 70/3/8916. A.P. is co-funded by the Foundation for Education and European Culture (IPEP).

(C) Schematic representation of *m*-GLF16 internalization and lipofuscin detection. M-GLF16 can enter the cell membrane and due to the pH difference between the intracellular and extracellular environment, it allows the controlled release of GLF16 that subsequently detects and binds to lipofuscin, inducing the detectable fluorescent signal.

(D) Schematic of the experimental process validating *m*-GLF16 incorporation in Li-Fraumeni-p21$^{WAF1/Cip1}$ Tet-ON cells through live cell FACS sorting and immunofluorescence.

(E) Proper internalization of *m*-GLF16 and specific labeling of live senescent cells was validated by flow cytometry and immunofluorescence. Representative pictures (left) and quantification (right) of analysis. Data presented as mean ± SD from three independent experiments. Objectives 20×. Scale bar, 25 μm. $^{**}p < 0.01$, $^{***}p < 0.001$ compared to (−) doxycycline by two-tailed Students' t test.

(F) Left panel: heatmap depicting the differentially expressed genes (DEGs) of live-sorted GLF16 (+) against GLF16 (−) cells. Right panel: part of the DEGs heatmap displaying the most significant senescence signature genes (DEGs cut-off: Log2 fold change 0.5, p value < 0.05).

(G) Left panel: pie charts showing the genomic distribution of the accessible regions of induced and repressed H3K27ac ChIP-seq peaks. Right panel: density heatmaps of the differentially accessible regions of live-sorted GLF16 (+) against GLF16 (−) cells. The reference point for the plotting is the center of the peaks (CoP), with distance 2.5 kb downstream and upstream of the peaks.

(H) Venn diagram depicting the overlap of significantly upregulated genes with genes assigned to H3K27ac ChIP-seq peaks in live GLF16 (+) versus GLF16 (−) cells (distance: −100/+25 kb from TSS, p value represents hypergeometric test). The table shows examples of upregulated senescence-associated genes with identified higher H3K27ac ChIP-seq peaks. The bedgraphs display differences in the H3K27ac ChIP-seq signal of representative senescence-associated genes in GLF16 (+) and GLF16 (−) cells and their corresponding inputs.

(I) Venn diagram depicting the overlap of significantly downregulated genes with genes assigned to repressed H3K27ac ChIP-seq peaks in live GLF16 (+) versus GLF16 (−) cells (distance: −100/+25 kb from TSS, p value represents hypergeometric test). The table shows examples of downregulated senescence-associated genes with identified repressed H3K27ac regions. The bedgraphs display differences in the H3K27ac ChIP-seq signal of a representative senescence-associated gene in GLF16 (+) and GLF16 (−) cells and their corresponding inputs.

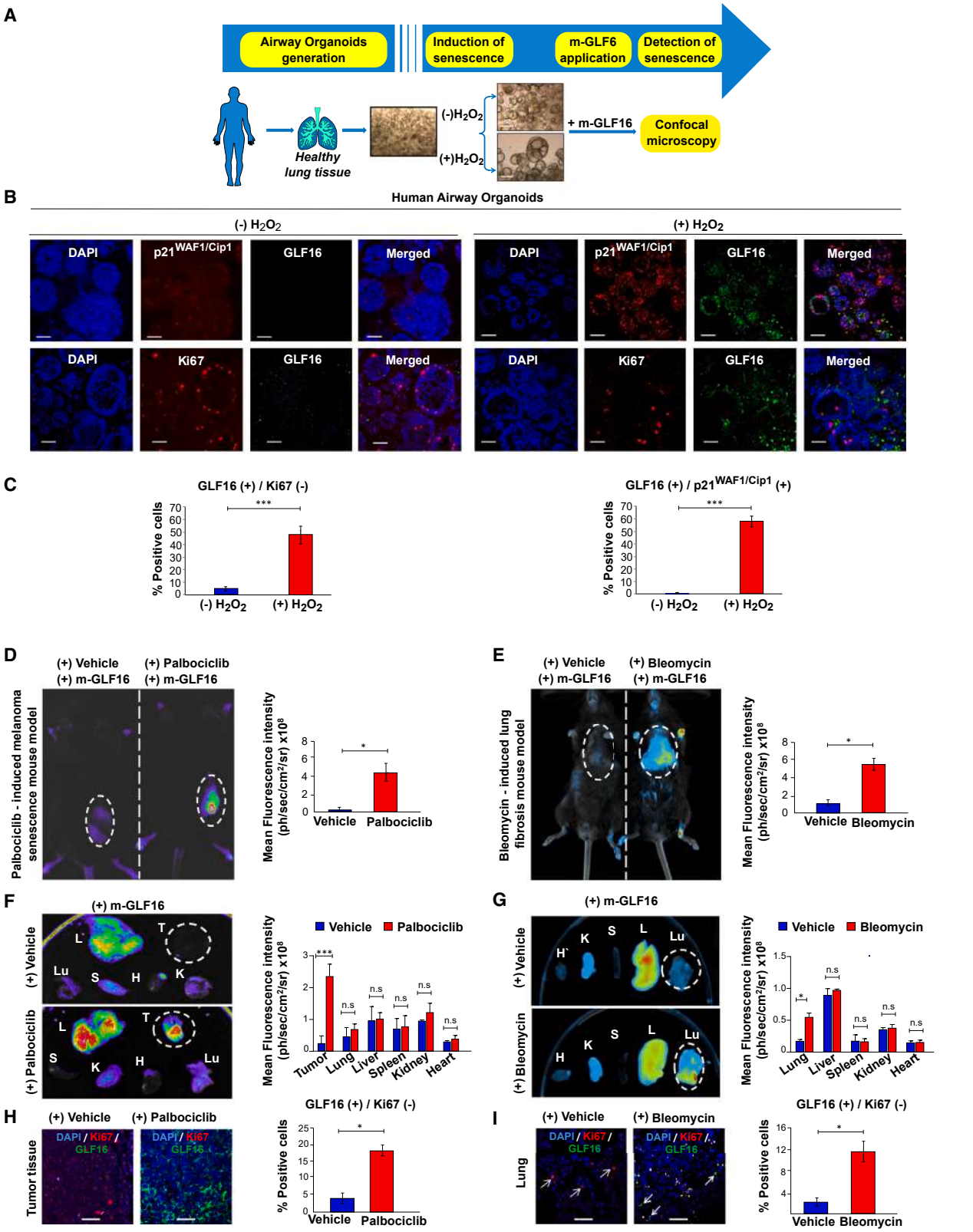

(legend on next page)

J.B and P.G. received funding from the Danish Cancer Society (R167-A11068 and R204-A12617-B153), the Lundbeck Foundation (R266-2017-4289 and R322-2019-2577), the Novo Nordisk Foundation (NNF20OC0060590), the Swedish Research Council (VR-MH 2014-46602-117891-30), the Danish Council for Independent Research (DFF-7016-00313), and the Danish National Research Foundation (project CARD, DNRF 125).

AUTHOR CONTRIBUTIONS

D.V. and K.K.: immunofluorescence; K.E. and V.G.G.: histopathological examination and staining evaluation; S.M., D.V., and P.V.: flow cytometry, FACS; P.G.: QIBC analysis; S.M. and D.V.: cell culture and murine models; S.M. and D.V.: *in vivo* imaging; V.G.G. and N.L.: chemical design of GLF16 and its structural analogs; Athanasios P., M.G., Nicole P., P.M., and N.L.: chemical synthesis of GLF16 and its structural analogs, determination of melting points, ^{1}H NMR spectra, ^{13}C NMR spectra and 2D spectra, mass spectra, absorption/emission spectra, flash chromatography, TLC analyses; N.P., Nefeli L., and C.D.: micelle design; N.P. and Nefeli L.: micelle characterization; S.P., M.C., and N.P.: micelle synthesis; S.M. and D.V.: micelle validation; Dimitrios V., G.V., and D.T.: RNA-seq; S.F., A.M., Aikaterini P., G.V., and D.T.: ChIP-seq; Aikaterini P.: bioinformatic analyses; A.P.: organoid isolation, development and micelle incorporation; S.M., D.V., A.P., Nefeli L., K.E., and A.K.: data analysis, statistical analysis, interpretation of results and manuscript preparation; D.T., C.R., J.B., R.P., M.S., M.D., K.E., and V.G.G.: experimental design and guidance; K.E., A.K., and V.G.G.: manuscript writing with input from all co-authors; V.G.G.: project conceptualization, resources, funding, and supervision of experiments.

DECLARATION OF INTERESTS

Pending patents: (1) Greek Patent Application 20230100019 and (2) University of Dundee 20230100019, regarding SBB analogs hydrophilic compounds on chemical synthesis, method(s), and application(s) use. M.S. is shareholder of Altos Labs, Senolytic Therapeutics, Life Biosciences, and Rejuveron Senescence Therapeutics, and was consultant, until the end of 2022, for Altos Labs and Rejuveron Senescence Therapeutics.

INCLUSION AND DIVERSITY

We support inclusive, diverse, and equitable conduct of research.

Received: January 23, 2023
Revised: July 31, 2023
Accepted: September 7, 2023
Published: October 5, 2023

REFERENCES

1. Gorgoulis, V., Adams, P.D., Alimonti, A., Bennett, D.C., Bischof, O., Bishop, C., Campisi, J., Collado, M., Evangelou, K., Ferbeyre, G., et al. (2019). Cellular Senescence: Defining a Path Forward. Cell *179*, 813–827. https://doi.org/10.1016/j.cell.2019.10.005.
2. Halazonetis, T.D., Gorgoulis, V.G., and Bartek, J. (2008). An oncogene-induced DNA damage model for cancer development. Science *319*, 1352–1355. https://doi.org/10.1126/science.1140735.
3. Gorgoulis, V.G., and Halazonetis, T.D. (2010). Oncogene-induced senescence: the bright and dark side of the response. Curr. Opin. Cell Biol. *22*, 816–827. https://doi.org/10.1016/j.ceb.2010.07.013.
4. Berlanga-Acosta, J.A., Guillén-Nieto, G.E., Rodríguez-Rodríguez, N., Mendoza-Mari, Y., Bringas-Vega, M.L., Berlanga-Saez, J.O., García Del Barco Herrera, D., Martinez-Jimenez, I., Hernandez-Gutierrez, S., and Valdés-Sosa, P.A. (2020). Cellular Senescence as the Pathogenic Hub of Diabetes-Related Wound Chronicity. Front. Endocrinol. *11*, 573032. https://doi.org/10.3389/fendo.2020.573032.
5. Evangelou, K., Veroutis, D., Paschalaki, K., Foukas, P.G., Lagopati, N., Dimitriou, M., Papaspyropoulos, A., Konda, B., Hazapis, O., Polyzou, A., et al. (2022). Pulmonary infection by SARS-CoV-2 induces senescence accompanied by an inflammatory phenotype in severe COVID-19: possible implications for viral mutagenesis. Eur. Respir. J. *60*, 2102951. https://doi.org/10.1183/13993003.02951-2021.
6. Evangelou, K., Vasileiou, P.V.S., Papaspyropoulos, A., Hazapis, O., Petty, R., Demaria, M., and Gorgoulis, V.G. (2023). Cellular senescence and cardiovascular diseases: moving to the "heart" of the problem. Physiol. Rev. *103*, 609–647.
7. Rodier, F., and Campisi, J. (2011). Four faces of cellular senescence. J. Cell Biol. *192*, 547–556. https://doi.org/10.1152/physrev.00007.2022.
8. Muñoz-Espín, D., and Serrano, M. (2014). Cellular senescence: from physiology to pathology. Nat. Rev. Mol. Cell Biol. *15*, 482–496. https://doi.org/10.1038/nrm3823.
9. Georgakopoulou, E.A., Tsimaratou, K., Evangelou, K., Fernandez Marcos, P.J., Zoumpourlis, V., Trougakos, I.P., Kletsas, D., Bartek, J., Serrano, M., and Gorgoulis, V.G. (2013). Specific lipofuscin staining as a novel biomarker to detect replicative and stress-induced senescence. A method applicable in cryo-preserved and archival tissues. Aging *5*, 37–50. https://doi.org/10.18632/aging.100527.
10. Hanahan, D. (2022). Hallmarks of Cancer: New Dimensions. Cancer Discov. *12*, 31–46. https://doi.org/10.1158/2159-8290.CD-21-1059.
11. Kohli, J., Wang, B., Brandenburg, S.M., Basisty, N., Evangelou, K., Varela-Eirin, M., Campisi, J., Schilling, B., Gorgoulis, V., and Demaria, M. (2021). Algorithmic assessment of cellular senescence in experimental and clinical specimens. Nat. Protoc. *16*, 2471–2498. https://doi.org/10.1038/s41596-021-00505-5.
12. Colas, K., Doloczki, S., Kesidou, A., Sainero-Alcolado, L., Rodriguez-Garcia, A., Arsenian-Henriksson, M., Dyrager, C., and Dyrager, C. (2021). Photophysical Characteristics of Polarity-Sensitive and Lipid. ChemPhotoChem *5*, 632–643. https://doi.org/10.1002/cptc.202100040.
13. Galanos, P., Vougas, K., Walter, D., Polyzos, A., Maya-Mendoza, A., Haagensen, E.J., Kokkalis, A., Roumelioti, F.M., Gagos, S., Tzetis, M., et al. (2016). Chronic p53-independent p21 expression causes genomic instability by deregulating replication licensing. Nat. Cell Biol. *18*, 777–789. https://doi.org/10.1038/ncb3378.

Figure 7. *m*-GLF16 identifies senescent cells *in vivo*

(A) Airway organoids were generated from surgically resected healthy lung tissues. Cultures were treated with hydrogen peroxide (H_2O_2) and incubated with *m*-GLF16, to allow organoid delivery.

(B) Selective incorporation of *m*-GLF16 in senescent cells was validated by confocal microscopy as indicated. Scale bars, 50–100 μm.

(C) Proper staining of senescent cells was verified by co-staining with $p21^{WAF1/Cip1}$. Data presented as mean ± SD from three independent experiments, ***$p < 0.001$ compared to (−) H_2O_2 by two-tailed Student's *t* test. Objectives 20×. Scale bar, 25 μm.

(D–I) *In vivo* tracking of senescent cells in senescence-associated murine models. Melanoma bearing mice were treated with vehicle or palbociclib for 7 consecutive days (D, F, and H). Alternatively, bleomycin was administered intratracheally in mice to develop lung fibrosis (E, G, and I).

(D and E) Mice were imaged 24 h after *m*-GLF16 was intravenously injected and fluorescence was quantified.

(F and G) Upon imaging, mice were euthanized and vital organs were harvested, imaged, and fluorescence was quantified. Lu = lungs, S = spleen, T = tumor, L = liver, K = kidney, and H = heart.

(H and I) Senescence-rich tissues as revealed by *in vivo* imaging were subsequently embedded in paraffin and validated for the presence of senescent cells by Ki67 and GLF16 staining. Data presented as mean ± SD, n = 5, *$p < 0.01$ compared to indicated controls.

14. Komseli, E.S., Pateras, I.S., Krejsgaard, T., Stawiski, K., Rizou, S.V., Polyzos, A., Roumelioti, F.M., Chiourea, M., Mourkioti, I., Paparouna, E., et al. (2018). A prototypical non-malignant epithelial model to study genome dynamics and concurrently monitor micro-RNAs and proteins in situ during oncogene-induced senescence. BMC Genom. *19*, 37. https://doi.org/10.1186/s12864-017-4375-1.

15. Evangelou, K., Lougiakis, N., Rizou, S.V., Kotsinas, A., Kletsas, D., Muñoz-Espín, D., Kastrinakis, N.G., Pouli, N., Marakos, P., Townsend, P., et al. (2017). Robust, universal biomarker assay to detect senescent cells in biological specimens. Aging Cell *16*, 192–197. https://doi.org/10.1111/acel.12545.

16. Li, Y., Sun, Y., Li, J., Su, Q., Yuan, W., Dai, Y., Han, C., Wang, Q., Feng, W., and Li, F. (2015). Ultrasensitive near-infrared fluorescence-enhanced probe for in vivo nitroreductase imaging. J. Am. Chem. Soc. *137*, 6407–6416. https://doi.org/10.1021/jacs.5b04097.

17. Ren, T.B., Xu, W., Zhang, W., Zhang, X.X., Wang, Z.Y., Xiang, Z., Yuan, L., and Zhang, X.B. (2018). A General Method To Increase Stokes Shift by Introducing Alternating Vibronic Structures. J. Am. Chem. Soc. *140*, 7716–7722. https://doi.org/10.1021/jacs.8b04404.

18. Zampetidis, C.P., Galanos, P., Angelopoulou, A., Zhu, Y., Polyzou, A., Karamitros, T., Kotsinas, A., Lagopati, N., Mourkioti, I., Mirzazadeh, R., et al. (2021). A recurrent chromosomal inversion suffices for driving escape from oncogene-induced senescence via subTAD reorganization. Mol. Cell *81*, 4907–4923.e8. https://doi.org/10.1016/j.molcel.2021.10.017.

19. Lieschke, E., Wang, Z., Chang, C., Weeden, C.E., Kelly, G.L., and Strasser, A. (2022). Flow cytometric single cell-based assay to simultaneously detect cell death, cell cycling, DNA content and cell senescence. Cell Death Differ. *29*, 1004–1012. https://doi.org/10.1038/s41418-022-00964-7.

20. Noppe, G., Dekker, P., de Koning-Treurniet, C., Blom, J., van Heemst, D., Dirks, R.W., Tanke, H.J., Westendorp, R.G.J., and Maier, A.B. (2009). Rapid flow cytometric method for measuring senescence associated beta-galactosidase activity in human fibroblasts. Cytometry A. *75*, 910–916. https://doi.org/10.1002/cyto.a.20796.

21. Kim, K.M., Noh, J.H., Bodogai, M., Martindale, J.L., Yang, X., Indig, F.E., Basu, S.K., Ohnuma, K., Morimoto, C., Johnson, P.F., et al. (2017). Identification of senescent cell surface targetable protein DPP4. Genes Dev. *31*, 1529–1534. https://doi.org/10.1101/gad.302570.117.

22. Papaspyropoulos, A., Hazapis, O., Altulea, A., Polyzou, A., Verginis, P., Evangelou, K., Fousteri, M., Papantonis, A., Demaria, M., and Gorgoulis, V. (2023). Decoding of translation-regulating entities reveals heterogeneous translation deficiency patterns in cellular senescence. Aging Celle13893. https://doi.org/10.1111/acel.13893.

23. Sachs, N., Papaspyropoulos, A., Zomer-van Ommen, D.D., Heo, I., Böttinger, L., Klay, D., Weeber, F., Huelsz-Prince, G., Iakobachvili, N., Amatngalim, G.D., et al. (2019). Long-term expanding human airway organoids for disease modeling. EMBO J. *38*, e100300. https://doi.org/10.15252/embj.2018100300.

24. Papaspyropoulos, A., Tsolaki, M., Foroglou, N., and Pantazaki, A.A. (2020). Modeling and Targeting Alzheimer's Disease With Organoids. Front. Pharmacol. *11*, 396. https://doi.org/10.3389/fphar.2020.00396.

25. Kim, J., Koo, B.K., and Knoblich, J.A. (2020). Human organoids: model systems for human biology and medicine. Nat. Rev. Mol. Cell Biol. *21*, 571–584. https://doi.org/10.1038/s41580-020-0259-3.

26. Dimozi, A., Mavrogonatou, E., Sklirou, A., and Kletsas, D. (2015). Oxidative stress inhibits the proliferation, induces premature senescence and promotes a catabolic phenotype in human nucleus pulposus intervertebral disc cells. Eur. Cell. Mater. *30*, 89–103. https://doi.org/10.22203/ecm.v030a07.

27. Vilgelm, A.E., Johnson, C.A., Prasad, N., Yang, J., Chen, S.C., Ayers, G.D., Pawlikowski, J.S., Raman, D., Sosman, J.A., Kelley, M., et al. (2016). Connecting the Dots: Therapy-Induced Senescence and a Tumor-Suppressive Immune Microenvironment. J. Natl. Cancer Inst. *108*, djv406. https://doi.org/10.1093/jnci/djv406.

28. Aoshiba, K., Tsuji, T., and Nagai, A. (2003). Bleomycin induces cellular senescence in alveolar epithelial cells. Eur. Respir. J. *22*, 436–443. https://doi.org/10.1183/09031936.03.00011903.

29. Tsaioun, K., Blaauboer, B.J., and Hartung, T. (2016). Evidence-based absorption, distribution, metabolism, excretion (ADME) and its interplay with alternative toxicity methods. ALTEX *33*, 343–358. https://doi.org/10.14573/altex.1610101.

30. Bartkova, J., Rezaei, N., Liontos, M., Karakaidos, P., Kletsas, D., Issaeva, N., Vassiliou, L.V.F., Kolettas, E., Niforou, K., Zoumpourlis, V.C., et al. (2006). Oncogene-induced senescence is part of the tumorigenesis barrier imposed by DNA damage checkpoints. Nature *444*, 633–637. https://doi.org/10.1038/nature05268.

31. Pakuła, M., Mały, E., Uruski, P., Witucka, A., Bogucka, M., Jaroszewska, N., Makowska, N., Niklas, A., Moszyński, R., Sajdak, S., et al. (2020). Deciphering the Molecular Mechanism of Spontaneous Senescence in Primary Epithelial Ovarian Cancer Cells. Cancers *12*, 296. https://doi.org/10.3390/cancers12020296.

32. Ruhland, M.K., Loza, A.J., Capietto, A.H., Luo, X., Knolhoff, B.L., Flanagan, K.C., Belt, B.A., Alspach, E., Leahy, K., Luo, J., et al. (2016). Stromal senescence establishes an immunosuppressive microenvironment that drives tumorigenesis. Nat. Commun. *7*, 11762. https://doi.org/10.1038/ncomms11762.

33. Mikuła-Pietrasik, J., Uruski, P., Sosińska, P., Maksin, K., Piotrowska-Kempisty, H., Kucińska, M., Murias, M., Szubert, S., Woźniak, A., Szpurek, D., et al. (2016). Senescent peritoneal mesothelium creates a niche for ovarian cancer metastases. Cell Death Dis. *7*, e2565. https://doi.org/10.1038/cddis.2016.417.

34. Chountoulesi, M., Perinelli, D.R., Forys, A., Katifelis, H., Selianitis, D., Chrysostomou, V., Lagopati, N., Bonacucina, G., Trzebicka, B., Gazouli, M., et al. (2022). Studying the properties of polymer-lipid nanostructures: The role of the host lipid. J. Drug Deliv. Sci. Technol. *77*, 103830. https://doi.org/10.1016/j.jddst.2022.103830.

35. Lagopati, N., Efstathopoulos, E.P., Veroutis, D., Katifelis, H., Theocharous, G., Pantelis, P., Evangelou, K., Gorgoulis, V.G., and Gazouli, M. (2022). Hybrid Multifunctional Nanomaterials for Diagnostic and Therapeutic Applications. In Pharmaceutical Nanobiotechnology for Targeted Therapy, Nanotechnology in the Life Sciences, Springer Nature Switzerland AG, H. Barabadi, E. Mostafavi, and M. Saravanan, eds.

36. Lagopati, N., Evangelou, K., Falaras, P., Tsilibary, E.P.C., Vasileiou, P.V.S., Havaki, S., Angelopoulou, A., Pavlatou, E.A., and Gorgoulis, V.G. (2021). Nanomedicine: Photo-activated nanostructured titanium dioxide, as a promising anticancer agent. Pharmacol. Ther. *222*, 107795. https://doi.org/10.1016/j.pharmthera.2020.107795.

37. Pippa, N., Kaditi, E., Pispas, S., and Demetzos, C. (2013). PEO-b-PCL–DPPC chimeric nanocarriers: self-assembly aspects in aqueous and biological media and drug incorporation. Soft Matter *9*, 4073–4082. https://doi.org/10.1039/C3SM27447K.

38. Chroni, A., Mavromoustakos, T., and Pispas, S. (2020). Biocompatible PEO-b-PCL Nanosized Micelles as Drug Carriers: Structure and Drug-Polymer Interactions. Nanomaterials *10*, 1872. https://doi.org/10.3390/nano10091872.

39. Brandt, J.V., Piazza, R.D., Dos Santos, C.C., Vega-Chacón, J., Amantéa, B.E., Pinto, G.C., Magnani, M., Piva, H.L., Tedesco, A.C., Primo, F.L., et al. (2019). Synthesis and colloidal characterization of folic acid-modified PEG-b-PCL Micelles for methotrexate delivery. Colloids Surf. B Biointerfaces *177*, 228–234. https://doi.org/10.1016/j.colsurfb.2019.02.008.

40. Galanos, P., Pappas, G., Polyzos, A., Kotsinas, A., Svolaki, I., Giakoumakis, N.N., Glytsou, C., Pateras, I.S., Swain, U., Souliotis, V.L., et al. (2018). Mutational signatures reveal the role of RAD52 in p53-independent p21-driven genomic instability. Genome Biol. *19*, 37. https://doi.org/10.1186/s13059-018-1401-9.

41. Langmead, B., and Salzberg, S.L. (2012). Fast gapped-read alignment with Bowtie 2. Nat. Methods *9*, 357–359. https://doi.org/10.1038/nmeth.1923.

42. Dobin, A., Davis, C.A., Schlesinger, F., Drenkow, J., Zaleski, C., Jha, S., Batut, P., Chaisson, M., and Gingeras, T.R. (2013). STAR: ultrafast universal RNA-seq aligner. Bioinformatics *29*, 15–21. https://doi.org/10.1093/bioinformatics/bts635.

43. Li, H., Handsaker, B., Wysoker, A., Fennell, T., Ruan, J., Homer, N., Marth, G., Abecasis, G., and Durbin, R.; 1000 Genome Project Data Processing Subgroup (2009). The Sequence Alignment/Map format and SAMtools. Bioinformatics *25*, 2078–2079. https://doi.org/10.1093/bioinformatics/btp352.

44. Anders, S., Pyl, P.T., and Huber, W. (2015). HTSeq–a Python framework to work with high-throughput sequencing data. Bioinformatics *31*, 166–169. https://doi.org/10.1093/bioinformatics/btu638.

45. Risso, D., Ngai, J., Speed, T.P., and Dudoit, S. (2014). Normalization of RNA-seq data using factor analysis of control genes or samples. Nat Biotech *32*, 896–902. https://doi.org/10.1038/nbt.2931.

46. Love, M.I., Huber, W., and Anders, S. (2014). Moderated estimation of fold change and dispersion for RNA-seq data with DESeq2. Genome Biol. *15*, 550. https://doi.org/10.1186/s13059-014-0550-8.

47. Zhang, Y., Liu, T., Meyer, C.A., Eeckhoute, J., Johnson, D.S., Bernstein, B.E., Nusbaum, C., Myers, R.M., Brown, M., Li, W., and Liu, X.S. (2008). Model-based analysis of ChIP-Seq (MACS). Genome Biol. *9*, R137. https://doi.org/10.1186/gb-2008-9-9-r137.

48. Chang, W., Cheng, J., Allaire, J., Sievert, C., Schloerke, B., Xie, Y., Allen, J., McPherson, J., Dipert, A., and Borges, B. (2023). shiny: Web Application Framework for R. R package version 1.7.4.9001. https://shiny.rstudio.com/.

49. Quinlan, A.R., and Hall, I.M. (2010). BEDTools: a flexible suite of utilities for comaring genomic features. Bioinformatics *26*, 841–842. https://doi.org/10.1093/bioinformatics/btq033.

50. Ramírez, F., Dündar, F., Diehl, S., Grüning, B.A., and Manke, T. (2014). deepTools: a flexible platform for exploring deep-sequencing data. Nucl. Acids Res. *42*. W187–91. https://doi.org/10.1093/nar/gku365.

51. Robinson, M.D., McCarthy, D.J., and Smyth, G.K. (2010). edgeR: a Bioconductor package for differential expression analysis of digital gene expression data. Bioinformatics *26*, 139–140. https://doi.org/10.1093/bioinformatics/btp616.

52. Liakou, E., Mavrogonatou, E., Pratsinis, H., Rizou, S., Evangelou, K., Panagiotou, P.N., Karamanos, N.K., Gorgoulis, V.G., and Kletsas, D. (2016). Ionizing radiation-mediated premature senescence and paracrine interactions with cancer cells enhance the expression of syndecan 1 in human breast stromal fibroblasts: the role of TGF-β. Aging *8*, 1650–1669. https://doi.org/10.18632/aging.100989.

53. Petrakis, T.G., Komseli, E.S., Papaioannou, M., Vougas, K., Polyzos, A., Myrianthopoulos, V., Mikros, E., Trougakos, I.P., Thanos, D., Branzei, D., et al. (2016). Exploring and exploiting the systemic effects of deregulated replication licensing. Sem Cancer Biol *37–38*, 3–15. https://doi.org/10.1016/j.semcancer.2015.12.002.

54. Liontos, M., Koutsami, M., Sideridou, M., Evangelou, K., Kletsas, D., Levy, B., Kotsinas, A., Nahum, O., Zoumpourlis, V., Kouloukoussa, M., et al. (2007). Deregulated overexpression of hCdt1 and hCdc6 promotes malignant behavior. Cancer Res. *67*, 10899–10909. https://doi.org/10.1158/0008-5472.CAN-07-2837.

55. Liontos, M., Niforou, K., Velimezi, G., Vougas, K., Evangelou, K., Apostolopoulou, K., Vrtel, R., Damalas, A., Kontovazenitis, P., Kotsinas, A., et al. (2009). Modulation of the E2F1-driven cancer cell fate by the DNA damage response machinery and potential novel E2F1 in osteosarcomas. Am. J. Pathol. *175*, 376–391. https://doi.org/10.2353/ajpath.2009.081160.

56. Hellevik, T., and Martinez-Zubiaurre, I. (2014). Radiotherapy and the tumor stroma: the importance of dose and fractionation. Front. Oncol. *4*, 1. https://doi.org/10.3389/fonc.2014.00001.

57. Dai, H., Chen, R., Gui, C., Tao, T., Ge, Y., Zhao, X., Qin, R., Yao, W., Gu, S., Jiang, Y., and Gui, J. (2020). Eliminating senescent chondrogenic progenitor cells enhances chondrogenesis under intermittent hydrostatic pressure for the treatment of OA. Stem Cell Res. Ther. *11*, 199. https://doi.org/10.1186/s13287-020-01708-5.

58. Lagopati, N., Kitsiou, P.V., Kontos, A.I., Venieratos, P., Kotsopoulou, E., Kontos, A.G., Dionysiou, D.D., Pispas, S., Tsilibary, E.C., and Falaras, P. (2010). Photo-induced treatment of breast epithelial cancer cells using nanostructured titanium dioxide solution. J. Photochem. Photobiol. Chem. *214*, 215–223. https://doi.org/10.1016/j.jphotochem.2010.06.031.

59. Lagopati, N., Kotsinas, A., Veroutis, D., Evangelou, K., Papaspyropoulos, A., Arfanis, M., Falaras, P., Kitsiou, P.V., Pateras, I., Bergonzini, A., et al. (2021). Biological Effect of Silver-modified Nanostructured Titanium Dioxide in Cancer. Cancer Genomics Proteomics *18*, 425–439. https://doi.org/10.21873/cgp.20269.

60. Pippa, N., Mariaki, M., Pispas, S., and Demetzos, C. (2014). Preparation, development and in vitro release evaluation of amphotericin B-loaded amphiphilic block copolymer vectors. Int. J. Pharm. *473*, 80–86. https://doi.org/10.1016/j.ijpharm.2014.07.001.

61. Schafer, M.J., White, T.A., Iijima, K., Haak, A.J., Ligresti, G., Atkinson, E.J., Oberg, A.L., Birch, J., Salmonowicz, H., Zhu, Y., et al. (2017). Cellular senescence mediates fibrotic pulmonary disease. Nat. Commun. *8*, 14532. https://doi.org/10.1038/ncomms14532.

62. Dennis, G., Jr., Sherman, B.T., Hosack, D.A., Yang, J., Gao, W., Lane, H.C., and Lempicki, R.A. (2003). DAVID: Database for Annotation, Visualization, and Integrated Discovery. Genome Biol. *4*, P3.

63. Agelopoulos, M., and Thanos, D. (2006). Epigenetic determination of a cell-specific gene expression program by ATF-2 and the histone variant macroH2A. EMBO J. *25*, 4843–4853. https://doi.org/10.1038/sj.emboj.7601364.

64. Heng, L., Handsaker, B., Wysoker, A., Fennell, T., Ruan, J., Homer, N., Marth, G., Abecasis, G., and Durbin, R. (2009). The Sequence Alignment/Map format and SAMtools. Bioinformatics *15*, 2078–2079. https://doi.org/10.1093/bioinformatics/btp352.

65. Ramírez, F., Dündar, F., Diehl, S., Grüning, B.A., and Manke, T. (2014). deepTools: a flexible platform for exploring deep-sequencing data. Nucleic Acids Res. *42*, 187–191. https://doi.org/10.1093/nar/gku365.

STAR★METHODS

KEY RESOURCES TABLE

REAGENT or RESOURCE	SOURCE	IDENTIFIER
Antibodies		
Mouse monoclonal anti-p21$^{WAF1/Cip1}$	Santa Cruz	Cat# sc-6246; RRID:AB_628073
Rabbit monoclonal anti-p21$^{WAF1/Cip1}$	Abcam	Cat# ab188224; RRID:AB_2734729
Rabbit polyclonal anti-p16^{INK4A}	Abcam	Cat# ab54210; RRID:
Rabbit monoclonal anti-Ki-67	Abcam	Cat# ab16667, RRID:AB_302459
Goat anti-biotin	Biotium	Cat# 20055-1, RRID:AB_10853439
Alexa Fluor 488 goat anti-rabbit	Abcam	Cat# ab150077, RRID:AB_2630356
Alexa Fluor 568 goat anti-mouse	Abcam	Cat# ab175473, RRID:AB_2895153
Rat monoclonal anti-Ki-67	Biolegend	Cat# 151206, RRID:AB_2566801
Alexa Fluor 647 rabbit anti- p16^{INK4A}	Cell Signaling	Cat# 43161, RRID:AB_2799237
Rabbit monoclonal anti- p16^{INK4A}	Abcam	Cat# ab211542, RRID:AB_2891084
Rabbit polyclonal anti-Histone H3 (acetyl K27)	Abcam	Cat# ab4729, RRID:AB_2118291
Anti-CD3 (SP162 clone)	Abcam	Cat# ab135372, RRID:AB_2884903
Rabbit polyclonal anti- Cleaved Caspase-3	Cell Signaling	Cat# 9661, RRID:AB_2341188
APC anti-CD4	Biolegend	Cat#116013, RRID:AB_2563024
Biological samples		
Human Irradiated Head and Neck carcinomas	Evangelou et al. 2017[15]	N/A
Human Chemotherapy treated breast carcinomas	Evangelou et al. 2017[15]	N/A
Human liver tissue from young and aged patients	Evangelou et al. 2017[15]	N/A
Human seminal vesicles	Evangelou et al. 2017[15]	N/A
Mouse model conditionally expressing K-rasV12	Evangelou et al. 2017[15]	N/A
Mouse model of bleomycin induced lung fibrosis	Evangelou et al. 2017[15]	N/A
Palbociclib treated mouse tumor melanoma	Evangelou et al. 2017[15]	N/A
Chemicals, peptides, and recombinant proteins		
Doxycycline	Applichem	A2951; CAS: 24390-14-5
Keratinocyte-Serum Free medium	Invitrogen	17005–075
Dulbecco's Modified Eagle Medium (DMEM)	Thermo Fisher Scientific	11965092
Advanced DMEM/F-12	Thermo Fisher Scientific	12634010
Phosphate Buffer Saline (PBS) 1X	Biowest	L0615-500
Fetal Bovine Serum (FBS)	Thermo Fisher Scientific	10270–106
Bovine Serum Albumin (BSA)	Applichem	A1391; CAS: 9048-46-8
Tetracycline-free Fetal Bovine Serum	Biosera	FB-1001T/500
Paraformaldehyde (PFA)	Merck	104005; CAS: 30525-89-4
SenTraGor™	Lab Supplies Scientific	N/A
HPLC-grade water	Sigma-Aldrich	270733; CAS: 7732-18-5
Hydrogen peroxide solution	Sigma-Aldrich	H1009; CAS: 7722-84-1
Cultrex Basement Membrane Extract, PathClear	R&D Systems	3432-010-01
Cell Recovery Solution	Corning	354253

(*Continued on next page*)

Continued

REAGENT or RESOURCE	SOURCE	IDENTIFIER
Dasatinib	Tocris	6793; CAS: 302962-49-8
Quercetin	Sigma-Aldrich	1592409; CAS: 6151-25-3
Bleomycin (sulfate)	cayman	13877.5MG
Palbociclib	MedChemExpress	HY-50767
Thiazolyl Blue Tetrazolium Bromide	Sigma-Aldrich	M5655; CAS: 298-93-1
Mojosort Streptavidin-conjugated nanobeads	Biolegend	480016
Cisplatin	Sigma-Aldrich	232120
Diamidino-2-phenylindole (DAPI)	Thermo Fisher Scientific	62248
Chloroform	Sigma-Aldrich	02487; CAS: 67-66-3
Tween 20	Sigma-Aldrich	P1379; CAS: 9005-64-5
Glycine	Applichem	A1067; CAS 56-40-6
Triton X-100	Acros Organics	327372500
Sheep serum	Merck	S22-100ML
Proteinase K	Thermo Fisher Scientific	AM2548
Ampure XP purification beads	Beckman Coulter	20088800
Acetone	Sigma-Aldrich	179124; CAS: 67-64-1
Critical commercial assays		
TrueVIEW Autofluorescence Quenching Kit	Vector Laboratories	SP-8400-15
NucleoSpin totalRNA FFPE kit	Macherey-Nagel	740982.50
NucleoSpin RNA, Mini kit	Macherey-Nagel	740955.50
NEBNext® Ultra™ II Directional RNA Library Prep with Sample Purification Beads	New England Biolabs	E7765L
Deposited data		
Raw data	This paper	PRJNA925077
Raw data	This paper	PRJNA998465
Experimental models: Cell lines		
HBEC-CDC6 Tet-ON	Ramirez et al., 2003; Komseli et al., 2018[14]	Supplied by Liloglou T. (parental cells known as HBEC-3KT) Constructed by our group
Li-Fraumeni-p21$^{WAF1/Cip1}$ Tet-ON	Galanos P. et al. 2016[13]; Galanos P. et al. 2018[40]	Generated by our group
Airway organoids	This paper	Generated by our group
Primary murine splenocytes	This paper	Generated by our group
Experimental models: Organisms/strains		
Mouse: C57BL/6	BSRC Al. Fleming (Vari, Greece)	N/A
Software and algorithms		
FlowJo	–	–
ScanR	–	–
TIBCO	–	–
Kuant	–	–
Bowtie2 (v2.3.4.1)	Langmead and Salzberg, 2012[41]	https://sourceforge.net/projects/bowtie-bio/files/bowtie2/2.3.4.1/
STAR aligner (v 2.7.6a)	Dobin et al., 2013[42]	https://github.com/alexdobin/STAR
SAMtools (v1.7)	Li et al., 2009[43]	http://samtools.sourceforge.net/
HTseq count (v0.5.4p3.)	Anders et al., 2015[44]	https://htseq.readthedocs.io/en/master/history.html
RUVseq (v1.0.0)	Risso et al., 2014[45]	https://rdrr.io/bioc/RUVSeq/man/RUVr.html

(*Continued on next page*)

Continued

REAGENT or RESOURCE	SOURCE	IDENTIFIER
DESeq2	Love et al., 2014[46]	https://bioconductor.org/packages/release/bioc/html/DESeq2.html
MACS2 (v2.1.2)	Zhang et al., 2008[47]	https://pypi.org/project/MACS2/
Shiny(R package)	Chang et al., 2023[48]	https://cran.r-project.org/web/packages/shiny/index.html
BEDTools (v2.26.0)	Quinlan et al., 2010[49]	https://bedtools.readthedocs.io/en/latest/
DeepTools (v3.5.2)	Ramirez et al., 2014[50]	https://github.com/deeptools/deepTools
edgeR	Robinson et al., 2015[51]	https://bioconductor.org/packages/release/bioc/html/edgeR.html
Other		
Coverslips	Knittel Glass	302974
6-well plates	Greiner	657185

RESOURCE AVAILABILITY

Lead contact

Further information and requests for resources and reagents should be directed to and will be fulfilled by the lead contact, Dr. Vassilis Gorgoulis (vgorg@med.uoa.gr).

Materials availability

The compounds generated in this study and their protocol applications are available upon request from the lead contact, Dr. Vassilis Gorgoulis (vgorg@med.uoa.gr).

Data and code availability

- All RNA-seq and ChIP-seq data generated in this study have been deposited at the Database: Sequence Read Archive (SRA - https://www.ncbi.nlm.nih.gov/sra) with the accession numbers PRJNA925077 and PRJNA998465, respectively, and are publicly available as of the date of publication.
- No new code was generated in this study.
- Any additional information required to reanalyze the data reported in this paper is available from the lead contact upon request.

EXPERIMENTAL MODEL AND STUDY PARTICIPANT DETAILS

Models

A variety of biological materials that exhibit high levels of senescent cells were used as positive controls for validating the efficacy of the described analog to identify senescent cells.[15] We selected established *in vitro* and *in vivo* models as well as various clinical samples, that are known to exhibit robust cellular senescence, in response to stressful conditions (Stress Induced Senescence, SIPS), including oncogenic ones (Oncogene Induced Senescence, OIS).[9,30,40,52–56] GLF-16 was evaluated in the following models.

In vitro models

i) 2D: All *in vitro* experiments were conducted using the Li-Fraumeni-p21$^{WAF1/Cip1}$ Tet-ON and HBEC CDC6 Tet-ON cellular systems developed by our team, where senescence entry occurs upon Doxycycline induction.[13] Cells were maintained in DMEM (10% tetracycline free FBS) and induction of senescence was accomplished upon addition of Doxycycline (Applichem, Darmstadt, Germany) for 6 days as described previously.[13,18]

ii) Airway organoids (AO) were generated from surgically resected healthy lung tissue from NSCLC patients, and maintained in culture as previously described.[23]

In vivo models

Several human clinical samples and murine models known to demonstrate cellular senescence versus control tissues were used for GLF16 validation. The following models were analyzed as previously described[15]: i) Head and Neck tumor tissues (irradiated versus non irradiated), ii) Breast tissues (irradiated versus non irradiated), iii) Human liver tissue from young and aged patients, iv) Human seminal vesicles, v) Mouse model conditionally expressing K-ras^{V12}, vi) Mouse model of bleomycin induced pneumopathy and vii) palbociclib treated mouse tumor melanoma xenograft. Protocols for animal tissues and clinical sample collection, and their

experimental use were approved by the Bio-Ethics Committee of the Medical School of Athens, in accordance with the Declaration of Helsinki and local laws and regulations, following also written consent from the patients in the case of clinical samples.

METHOD DETAILS

GLF16 chemical synthesis

Synthesis of GLF16 and its structural analogues

In brief, the previously reported SBB lipophilic GL9 analogue (a non-biotinylated form of GL13) was used as lead compound and converted to the corresponding succinic ester GL353. GL353 was subsequently coupled with the synthesized cyanine heptamethine derivatives GLF6, GLF15, GLF18 and GLF20, leading eventually to the target derivatives GLF7, GLF16, GLF19 and GLF21, respectively. Detailed description concerning the synthetic procedures and the characterization of all these target derivatives is provided in Methods S1.

Poly(ethylene oxide)-block-poly(ε-caprolactone) (PEO-b-PCL) amphiphilic block copolymer preparation

The poly(ethylene oxide)-block-poly(ε-caprolactone) (PEO-b-PCL) amphiphilic block copolymer was prepared by ring opening polymerization of ε-caprolactone monomer using a monohydroxy terminated PEG (Sigma-Aldrich Chemical Co.) (M_n = 5,000) as the macroinitiator and stannous octanoate as the catalyst. The copolymer was characterized by size exclusion chromatography (SEC) and nuclear magnetic resonance (^{1}H-NMR) and it was found to have the following molecular characteristics: M_w = 10,600, 53 wt % PCL (hydrophobic component).[37] All formulations were prepared in HPLC-grade water, which was purchased from Sigma–Aldrich Chemical Co. Chloroform and acetone were of analytical grade and purchased from Sigma–Aldrich Chemical Co.

GLF16 solution preparation

4 mg of GLF16 were diluted in 500μL of DMSO (solution 1). Then 25 μL of solution 1 were mixed with an equal volume of Tween 20, and subsequently 950 μL of PBS were added to prepare a stock solution of 200 μg/ml (solution 2). Working solution for *in situ* fluorescence and flow cytometry experiments, was 70 μg/mL and 4–50 μg/mL (in 2.5% DMSO/2.5%/TWEEN 20/PBS), respectively.

Immunofluorescence analysis

Inducible Li Fraumeni-p21$^{WAF1/Cip1}$ Tet-ON and HBEC CDC6 Tet-ON cell lines were seeded (2x10^5 cells/well) on coverslips (12-mm diameter) and were subsequently triggered to senescence induction upon treatment with Doxycycline. Coverslips were removed, cells were fixed (4% PFA/PBS, 10min, 4°C) and permeabilized (Triton 0.3%/PBS 15 min). Blocking of non-specific epitopes was performed using sheep serum (S22, Merck Millipore). Cells were subsequently stained with primary antibodies for 1h, and positive cells were visualized using secondary antibodies for 1h. Upon staining with primary and secondary antibodies, cells were stained for lipofuscin using GLF16 for 10 min (70 μg/ml) avoiding light exposure. Excess compound was removed by washing thrice with the GLF16 diluent. Nuclei were finally visualized by DAPI staining. Cells were washed (30s with dH_2O) and coverslips were mounted onto slides for microscopy.

Formalin fixed paraffin embedded (FFPE) tissue sections (4μm) were de-parafinized, and rehydrated. Sections were immersed in citrate buffer (pH = 6) and antigenic epitopes retrieval was performed in a steamer for 15 min. Blocking of non-specific epitopes was performed using sheep serum (S22, Merck Millipore). GLF16 was applied for 10 min (100 μg/ml) avoiding light exposure. Section were washed 3 times for 10 min each with GLF16 dilutant. For double immunofluorescence staining, sections were incubated with primary antibodies were for 1h following GLF16 application and secondary antibodies were applied for 1h. Tissue autofluorescence was diminished using the TrueVIEW Autofluorescence Quenching Kit (Vector Laboratories Inc., CA, USA). SenTraGor staining was performed as previously described.[15] Sections were counterstained with DAPI and mounted. Sections were visualized using the Leica TCS-SP8 confocal microscope at 20x, 40x and 63x objectives. Evaluation of the staining outcome was carried out as previously described (Zampetidis et al.2021).

Flow cytometry

GLF16 was first validated using the Li-Fraumeni-p21$^{WAF1/Cip1}$ Tet-ON and HBEC CDC6 Tet-ON cellular systems. Cells were plated onto 10-cm cell culture dishes and treated with or without Doxycycline for cellular senescence induction. Cells were subsequently collected (centrifuged at 280 g), fixed with 4% paraformaldehyde solution for 15 min, washed with 1 mL PBS and subsequently permeabilized with 0.25% Triton X- for 15 min. Cells were washed again and stained for lipofuscin using 4–50 μg/mL GLF16 for 8 min. Excess compound was removed by washing twice with GLF16 solvent solution. Cells were subsequently stained with anti-p16^{INK4A}-APC (Cell Signaling Technology, Danvers, MA) and anti-Ki67-Pacific blue (Biolegend, San Diego, CA) antibodies.

To evaluate senescence in primary cultures, T cells were isolated from fresh murine spleens using anti-CD3 biotinylated antibody and streptavidin-conjugated magnetic beads (Mojosort kit, Biolegend, San Diego, CA). T cells were subsequently treated with vehicle (PBS) or cisplatin (50μM) overnight and cells were collected, washed and stained for lipofuscin as described above, and subsequently stained with anti-p16^{INK4A} (Abcam, Cambridge, UK) primary antibody for 30 min, followed by addition of Dylight 488 secondary antibody (Biolegend, San Diego, CA). In all cases cells were analyzed in a BD FACSCantoII flow cytometer and analyzed by FlowJo Software (LLC, Ashland, OR, USA). Gating strategy is displayed in Figure S5A.

QIBC analysis

Quantitative image-based cytometry (QIBC) analysis (Figure S2) was performed essentially as previously described.[18] In brief, images were taken with a ScanR inverted microscope High-content Screening Station (Olympus) for Life Science that was equipped with wide-field optics, 20x dry objectives were used, fast excitation and emission filter-wheel devices for 6 different spectral wavelength areas, an MT20 illumination system, and a digital monochrome scientific CMOS camera with sensor chip FL-400. Images were obtained in an automated fashion with the ScanR acquisition software (Olympus, 3.2.0). For each condition, 100 images were acquired containing at least 10,000 cells per condition. Acquisition times for the different channels were adjusted for nonsaturated conditions, and same settings were applied to all the samples within one experiment. Images were processed and analyzed with the corresponding ScanR analysis software. In brief, the DAPI signal was used for the generation of an intensity-threshold-based mask to identify individual nuclei as main objects. This mask was then applied to analyze pixel intensities in different channels for each individual nucleus. For analysis of GLF16, additional masks were generated by defining a 'ring' surrounding the mask (nuclei) and an automated detection of single nuclei with intensity-based or spot-detector modules provide by the software. The 'ring' was defined as sub-object, and the generated mask was used for quantification of pixel mean intensities in foci. Based on the distinguished objects and sub-objects, the desired parameters (mean and total intensities, area, foci count, and foci intensities) for the each nuclei or foci were quantified, as well as derived parameters (sum of mean intensity per nucleus-representing each cell). These values were then exported as.txt files and analyzed with TIBCO Software (version 10.10.0). This software was used to quantify absolute, median, and average values in cell populations and to generate all color-coded scatterplots. Within one experiment, similar cell numbers were compared for the different conditions.

Treatment with senolytics

Dasatinib (cat. No.6793, Tocris Bioscience, UK) and Quercetin (cat. No. 1592409, Sigma, USA) solutions were prepared as previously described.[57] Li-Fraumeni-p21$^{WAF1/Cip1}$ Tet-ON were treated with escalating concentrations of Dasatinib (0-20μM) and 15μM Quercetin (D + Q) for 3 subsequent days. MTT (3-(4,5-Dimethylthiazol-2-yl)-2,5-diphenyltetrazolium bromide) colorimetric assay (Thiazolyl Blue Tetrazolium Bromide, M5655, Sigma-Aldrich, Darmstadt, Germany) was applied for the estimation of cell viability after D + Q treatment as previously described.[58,59]

Nano-delivery system

Preparation of micelles

Polymeric micelles were prepared by the thin-film hydration method as previously described.[60] Detailed description regarding to the preparation of micelles PEO-b-PCL micelles is provided in Methods S3.

Physiochemical characterization

The physicochemical characteristics of the prepared nanosystems were evaluated by measuring their mean hydrodynamic diameter (Dh, nm) and polydispersity index (PDI) through Dynamic Light Scattering (DLS) and by morphological observation via Transmission Electron Microscopy (TEM). Detailed description concerning the characterization of pure PEO-b-PCL and *m*-GLF16 is provided in Methods S3.

m-GLF16 administration for fluorescence microscopy and flow cytometry

Li-Fraumeni-p21$^{WAF1/Cip1}$ Tet-ON cells were treated with 0.0125 μg/mL (Immunofluorescence) and 0.0166 μg/mL (Flow Cytometry) *m*-GLF16 for 3h (37°C, 5% CO_2) as the most effective, following testing at various concentrations and incubation time. Medium was subsequently removed, cells were washed twice with PBS and cells were either fixed with 4% PFA (10 min, 4°C), washed, stained with DAPI and observed via confocal microscopy, or collected and analyzed by flow cytometry.

Tracking of living senescent cells in human airway organoids using *m*-GLF16

For senescence induction, AO cultures were supplemented with 150 μM hydrogen peroxide (H_2O_2) for 72 h. At 24 and 48 h of treatment, the AO medium was removed and replaced by freshly H_2O_2-supplemented AO medium. Upon completion of treatment, organoids were left to grow in H_2O_2-free AO medium for 48 h. Next, H_2O_2-treated and control AO cultures were incubated with 0.125 μg/mL *m*-GLF16 for 3 h. For whole mount staining, AOs were removed from Basement Membrane Extract (BME; R&D systems) using Cell Recovery Solution (Corning), washed once with PBS and fixed for 20 min in 4% paraformaldehyde, permeabilized for 20 min in 0.2% Triton X-100 (Sigma), and blocked for 45 min in 1% BSA. AOs were incubated with primary antibody (p21$^{WAF1/Cip1}$; Cell Signaling) at 4°C overnight, washed with PBS three times, incubated with secondary antibody (Alexa Fluor 488) for 1h at RT, DAPI (1:1000; Biotium) was applied for 5 min, washed two times with PBS and mounted in anti-fade mounting medium. Samples were imaged on the Leica TCS-SP8 confocal microscope.

Visualization of senescent cells *in vivo*

C57BL/6 mice were purchased from BSRC Al. Fleming (Vari, Greece) and housed at the Animal Model Research Unit of Evangelismos Hospital. Mice received food and water *ad libitum*. Experiments were approved by the Veterinary Administration Bureau, Prefecture of Athens, Greece (Decision No: 548032, 08/05/2023) under compliance to the national law and the EU Directives. The potential of *m*-GLF16 to identify and visualize senescent cells *in vivo* was challenged in the palbociclib-treated mouse melanoma[27] and bleomycin-induced fibrosis[61] models known to exhibit robust senescence. Briefly, murine melanoma cells were subcutaneously

injected in the right flank of C57BL/6 mice and once tumors became palpable (6–8 days upon tumor cell inoculation), mice were administered 100 mg/kg of body weight of the CDK4/6 inhibitor (PD-0332991, palbociclib) by oral gavage for 7 consecutive days. In case of the bleomycin-induced pneumonopathy, C57BL6 mice were intra-tracheally administered with 2 units/kg of body weight to develop lung fibrosis. Senescence peaks from day 14–21.[61]

To monitor senescence *in vivo*, mice were intravenously injected with 1mg of *m*-GLF16 micellar dispersion under ketamine/xylazine anesthesia. Images were taken either using the small animal live optical-imaging φ-eye (Bioemtech, Athens, Greece) or Newton 7.0 Vilber Lourmat imager (Vilber, France) 24h upon *m*-GLF16 administration. For *ex vivo* validation of senescence, mice were euthanized and tumors (where applicable), heart, liver, lungs, spleen and kidneys were harvested and visualized immediately. Analysis of images was carried out using the Kuant software (Vilber, France). Fluorescence was measured in photons per second per square centimeter per steradian (ph/sec/cm2/sr) upon a selection of a region of interest area (ROI).

To additionally evaluate the toxicity of the compound, naive mice were administered with 1mg of *m*-GLF16 micellar dispersion intravenously, thrice every 2 h (in order to receive a high quantity of the micelle), and seven days later mice were euthanised, and blood and vital organs were collected. Total and differential WBC counts were determined using the Countess cell counter (Invitrogen) and blood smears were also evaluated upon May-Gruwald/Giemsa staining. Tissue sections of vital organs were stained for hematoxylin/eosin and assessed for histopathological alterations.

RNA and ChIP-sequencing analysis of fixed or live FACS-sorted cells

Cell preparation

Li-Fraumeni-p21$^{WAF1/Cip1}$ Tet-ON cells were seeded onto 10-cm cell culture plates and once they reached 70% confluency they were treated with 10 μg/mL Doxycycline for 6–8 days so that cells become senescent. Untreated cells were also cultured to serve as negative and unstained controls during the sorting analysis.

Cells were either fixed and stained with GLF16, or inoculated with *m*-GLF16 for 3h as described above. In both cases, GLF16+ cells were sorted against GLF16- using FACSAria II and collected in 5mL sterile, RNAse-free tubes.

RNA-seq analysis

Total mRNA from sorted cells was extracted using the NucleoSpin totalRNA FFPE kit (Macherey-Nagel, Germany) (in the case of fixed cells) or the NucleoSpin RNA mini kit (Macherey-Nagel, Germany) in the case of live cells. RNASEq libraries were prepared with the NEBNext ultra II **directional** RNASeq kit (Reverse strand specificity) and single-end sequenced at 101 bp length with the Illumina **NovaSeq 6000 platform**, in the Greek Genome Center of BRFAA.

Li-Fraumeni-p21$^{WAF1/Cip1}$ Tet-ON RNA-seq raw data were mapped to the human genome (version GRCh38/hg38) using STAR[42] aligner. Samtools[43] were used for data filtering and file format conversion, while the HT-seq count algorithm[44] was used to assign aligned reads to exons using the following command line "htseq-count –s no –m intersection –nonempty". Normalization of reads and removal of unwanted variation was performed with RUVseq.[45] Differentially expressed genes were identified using the DESeq2 R package[46] and genes with log2 fold change cut-off of 0.5 and p value less than 0.05 were considered to be significant. Gene ontology and pathway analysis was performed using the Database for Annotation, Visualization and Integrated Discovery (DAVID).[62] Only pathways and biological processes with p value less than 0.05 were considered to be significantly enriched. Heatmaps representing the significant differentially expressed genes and the most significant genes that constitute senescence signature were constructed with R package Shiny,[48] where hierarchical clustering was performed, with linkage method 'average'.

ChIP-seq analysis

For ChIP-seq analysis, samples were prepared using a previously published protocol[63] with certain modifications. Briefly, approximately 1 million cells per sample were fixed with 1% formaldehyde for 30 min at room temperature and quenched with 0.125M glycine for 5 min. After cell and nuclei lysis, chromatin was sonicated using a Covaris S220 instrument. In the immunoprecipitation step chromatin was incubated overnight with 3 μL (2 μg) of anti-H3K27ac antibody (Abcam, ab4729). Following immobilization on protein G beads and washing steps, samples were treated with proteinase K, crosslinks were reversed overnight at 65°C and the DNA was purified with Ampure XP purification beads (Macherey Nagel). Libraries were prepared using the NEBNext Ultra II DNA Library Prep Kit for Illumina following the kit instructions. To measure DNA concetration, a Qubit fluorometer was used and library sizes were assessed using the Agilent 2100 Bioanalyzer instrument. Samples were sequenced at the Greek Genome Center situated at BRFAA. H3K27ac ChIP-seq reads (single-end 100 bp reads and paired-end 65 bp reads) were generated with NovaSeq 6000. H3K27ac GLF16 (–) (three replicates) and H3K27ac GLF16 (+) (three replicates), H3K27ac *m*-GLF16 (–) (two replicates) and m-H3K27ac GLF16 (+) (two replicates) in Li-Fraumeni-p21$^{WAF1/CiP1}$ Tet-ON cells, with their corresponding inputs were aligned to the human genome (version GCCh38/hg38) with Bowtie2 algorithm[41] and «–verysensitive » parameter. Samtools[64] were used for data filtering and file format conversion. Duplicate reads, blacklist regions and chromosome M were removed before peak calling. The MACS2[47] algorithm with default q-value 0.01 was used for ChIP-seq peak identification. Accessible and non-accessible regions were identified from the narrowpeaks in two steps. First, the peak lists are merged to obtain consensus peaks with subcommands cat and mergeBed from BEDTools.[49] Second, with intersectBed and parameters –wa –u -v, we identify the new intersected peaks in order to identify the open and closed chromatin regions. The reads that belong to these consensus peaks are counted and a statistical model based on edgeR[51] is used for identifying the differential peaks. For the common peaks between two conditions, an extra analysis is done, with DESeq2,[46] which uses the Negative Binomial distribution to compute a p value and a fold change for each estimated peak. Peaks that are highly enriched in comparison with the rest are also considered as accessible regions.

Annotation of peaks to genes (100 kb upstream and 25 kb downstream of the TSS) and genomic distribution of accessible regions identified by MACS2 was performed using BEDTools and the -closestBed and -intersectBed subcommands, respectively. All bam files were converted to bedgraphs with genomeCoverageBed subcommand and using the -scale option. Density heatmaps were generated with the ComputeMatrix function from package DeepTools[65] and using a reference point with the parameters –referencePoint center -b 2500 -a 2500 -R <bed files> -S < bigwig files>. The function plotHeatmap from the same package was used for displaying the average profiles heatmaps. To check the statistical significance of the overlap between the assigned genes from peaks and the deregulated genes from RNA-seq, hypergeometric test was performed.

QUANTIFICATION AND STATISTICAL ANALYSIS

In each experiment, values are presented as means ± standard deviation. Differences between groups were evaluated using the parametric 2-tailed Student's *t* test, the non-parametric Mann Whitney or 1-way ANOVA with Bonferroni's post hoc test for multiple comparisons, as appropriate. $p < 0.05$ were considered significant. Statistical analysis was performed using the Statistical Package for the Social Sciences v.13.0.0 (IMB).

ADDITIONAL RESOURCES

For additional resources and information see supplemental information file and Methods S1, S2, and S3.